Cloud-Tracked Winds from *Pioneer Venus* OCPP Images

WILLIAM B. ROSSOW, ANTHONY D. DEL GENIO AND TIMOTHY EICHLER[†]

NASA Goddard Space Flight Center, Goddard Institute for Space Studies, New York, New York

(Manuscript received 9 May 1989, in final form 30 March 1990)

ABSTRACT

Analysis of ultraviolet image sequences, obtained from the *Pioneer Venus* Orbiter Cloud Photopolarimeter and covering five 80-day periods from 1979–1985, provides the first climatological description of the cloud top circulation on Venus. The average zonal winds can be characterized as a 5-day retrograde rotation of the whole cloud-level atmosphere with weak "jets" at middle to high latitudes. Both the midlatitude and equatorial zonal winds vary by about 5–8 m s^{-1} over time spans of 1–6 years. The average meridional circulation is poleward in both hemispheres up to at least 60° latitude, consistent with the presence of a thermally direct Hadley circulation associated with the clouds. The strength of the Hadley circulation also varies with time. Four wave modes are clearly identified: a diurnal solar tide, a semi-diurnal solar tide, a "4-day equatorial" wave, and a "5-day midlatitude" wave. The semidiurnal tide appears to have an amplitude of about 5 m s^{-1} and to be approximately constant with time; the diurnal tide varies in amplitude from about 10 m s^{-1} to less than 5 m s^{-1}. Both tides have phases such that maximum zonal windspeeds occur near the evening terminator. The "4-day" wave is wavenumber 1 and has an amplitude of about 5 m s^{-1} that peaks at the equator and varies with time; in 1982 no wave with this period was apparent in the data. This wave mode is identified as a Kelvin mode by Del Genio and Rossow. The "5-day" wave is wavenumber 1 and has an amplitude of about 5 m s^{-1} that peaks at midlatitudes and varies in time: in 1982 no wave with this period was apparent. This wave mode is identified as an internal Rossby–Haurwitz mode.

1. Introduction

Observations of the cloud-level motions on Venus have continued ever since the initial discovery of a quasi-periodic variation of the ultraviolet albedo (Boyer and Camichel 1961). Early spectroscopic measurements of windspeeds (Richardson 1958; Guinot and Feissel 1968) were ambiguous or in conflict and doubts about their accuracy were raised (Young 1974); however, doubts were also raised (Scott and Reese 1972; Beebe 1972) concerning the interpretation of the albedo periodicity as a bulk zonal flow at speeds near 100 m s^{-1} (Boyer and Guerin 1966, 1971; Smith 1967; Caldwell 1972). This interpretation has since been confirmed by better spectroscopic measurements (Traub and Carleton 1975; Betz et al. 1976) and by numerous in situ spacecraft observations (see Schubert 1983; Kerzhanovich and Marov 1983; Limaye 1985), including the two VEGA balloons (Sagdeev et al. 1986a). There is no doubt that the cloud level atmosphere superrotates at a speed about 50 times larger than the rotation rate of the solid body. Entry probe and remote observations also have shown that this superrotation involves the whole depth of the atmosphere, from at least about 10 km to about 100 km, at most latitudes (Schubert 1983). How the atmospheric circulation organizes itself to maintain such a momentum excess has remained one of the leading puzzles of atmospheric fluid dynamics (Rossow 1985).

Despite a long history of ground-based observations, the difficulties of measuring very small contrasts near the sun have only allowed for very episodic measurements of the periodicity of UV markings (Boyer and Camichel 1961; Boyer and Guerin 1966, 1971; Smith 1967; Caldwell 1972; Boyer 1973; Dollfus 1975). Recent measurements of changes in near-IR radiances have been interpreted as a bulk circulation at about 50 km altitude (Crisp et al. 1989). A series of nine *Venera* entry probes in the 1970s (Kerzhanovich and Marov 1983) provided only brief samples of the circulation that had large uncertainties and were limited to equatorial regions, with the exception of *Venera 9* (Marov and Moroz 1976). The *Mariner 10* mission acquired UV imaging data covering only about eight days (Suomi 1975; Belton et al. 1976a; Limaye and Suomi 1981). The four *Pioneer Venus* entry probes returned data in 1978 about the instantaneous vertical distributions of winds at three different latitudes and two longitudes from differential long-baseline interferometry (Counselman et al. 1980). The *Venera 11* and *12* entry probes also arrived at Venus in 1978 (Kerzhanovich et al. 1979); since then there have been only two

[†] ST Systems Corporation.

Corresponding author address: Dr. W. Rossow, NASA/GISS, 2880 Broadway, New York, NY 10025.

more *Venera* probes (Kerzhanovich et al. 1983). In 1985 two constant-pressure balloons were released near the equator at 56 km altitude and measured temperature, pressure, and relative windspeeds for two days (Sagdeev et al. 1986a, 1986b; Preston et al. 1986); the motions of these balloons were also tracked providing the first measurements of small scale turbulence in the Venus atmosphere (Linkin et al. 1986; Blamont et al. 1986).

All of these data represent only very sparse sampling of the total circulation of the Venus atmosphere. The only observations of instantaneous winds in any part of the Venus atmosphere with comprehensive space-time coverage are those obtained by the Orbiter Cloud Photo-polarimeter (OCPP) on the *Pioneer Venus* orbiter, which has collected data since late 1978 (Travis et al. 1979a, 1979b). The Radio Science dataset (Kliore and Patel 1980, 1982), which has collected temperature structure information over this same time period, has also been used to infer the average zonal flow over a broad range of altitudes (Newman et al. 1984; Walterscheid et al. 1985).

This paper and a companion (Del Genio and Rossow 1990, called DR90 in the remainder of the paper) describe the results of an analysis of OCPP imaging data, spanning nine years, to determine windspeeds at cloud level from the motions of UV cloud features. Early results have been reported for the first year of observations (Rossow et al. 1980) and from the first four years of measurements (Rossow 1985). Sufficient data were obtained over portions of the first seven years for tracking cloud feature motions; these are described in section 2. Section 3 describes the analysis method. An assessment of the measurement errors is given in section 4. The basic mean circulation inferred from this dataset and its variation over long time periods are presented in section 5, together with a discussion of wave motions identified in the data. A more detailed interpretation of the circulation is provided by combining these wind measurements with analysis of the variations of image brightness in DR90. Section 6 discusses the results and their implications.

2. Data

a. OCPP instrument

The OCPP is a six channel instrument on the *Pioneer Venus* Orbiter that observes Venus in spin–scan mode (Russell et al. 1977; Travis 1979; Travis et al. 1979a,b). The observations discussed here use data from one channel that measures UV (365 nm) radiances with about 30 km nadir resolution from the apoapsis portion of the Orbiter's highly elliptical 24 h period orbit. There is no systematic stepping of the telescope during imaging; instead the telescope is positioned and the orbital motion is used to scan across the planet, requiring about 4 h to complete one image. The 5 rpm spin rate of the spacecraft generates coverage of the planet in the other dimension. Images can be acquired during about 18 h out of each 24 h orbit. If this whole period is devoted to imaging, then four images per orbit are possible; however, collection of polarimetry data limits most imaging to two images per orbit. Telemetry constraints have limited the imaging frequency even further.

b. Imaging data

Since OCPP imaging uses reflected sunlight, imaging data are collected only for about 60–80 days every Venus year when the apoapsis portion of the orbit can view the sunlit side of Venus. Competition with other spacecraft for deep space network (DSN) coverage and interference of the sun have resulted in only a few good imaging periods over the last ten years. Figure 1 illustrates the imaging opportunities and shows the number of images and image pairs collected during each opportunity (note that one image can be in two pairs). Although the larger DSN antennas could have collected data at almost anytime, coverage was usually provided only by the smaller antennas and was, therefore, limited to the periods shown when Venus was close enough to Earth. The focus of our analysis is on the five imaging periods with a larger number of images in 1979, 1980, 1982, 1983 and 1985.

Pairs of images, separated by approximately four hours, are used to determine the motions at cloud top level by measuring displacements of the smaller cloud features (Rossow et al. 1980). Table 1 shows the total number of images and image pairs obtained in each imaging opportunity, together with the numbers of days with at least one image and at least one pair of images, and the average number of vectors obtained per day. Although some days have two image pairs in sequence, one pair per day is more typical. Table 2 shows the total number of vectors obtained for each imaging period as a function of latitude.

Feature contrasts range from a maximum of about 40% for the larger features to as little as 3% for the smallest features; instrument noise levels of about 1% allow for reliable detection of the smaller contrast features (Travis 1979). Use of an on-board calibration target also maintains knowledge of the radiances to within 6% (Travis 1979).

3. Tracking method

a. Overview description

Measuring windspeeds by tracking the motions of clouds in satellite images was first suggested for application to images of Earth (Hubert and Whitney 1971; Leese et al. 1971; Smith and Phillips 1972; Fujita et al. 1975). The basic premise is that "smaller" cloud features move with the bulk flow, whereas "larger" cloud features probably represent propagating, large scale waves. This method has been used extensively to

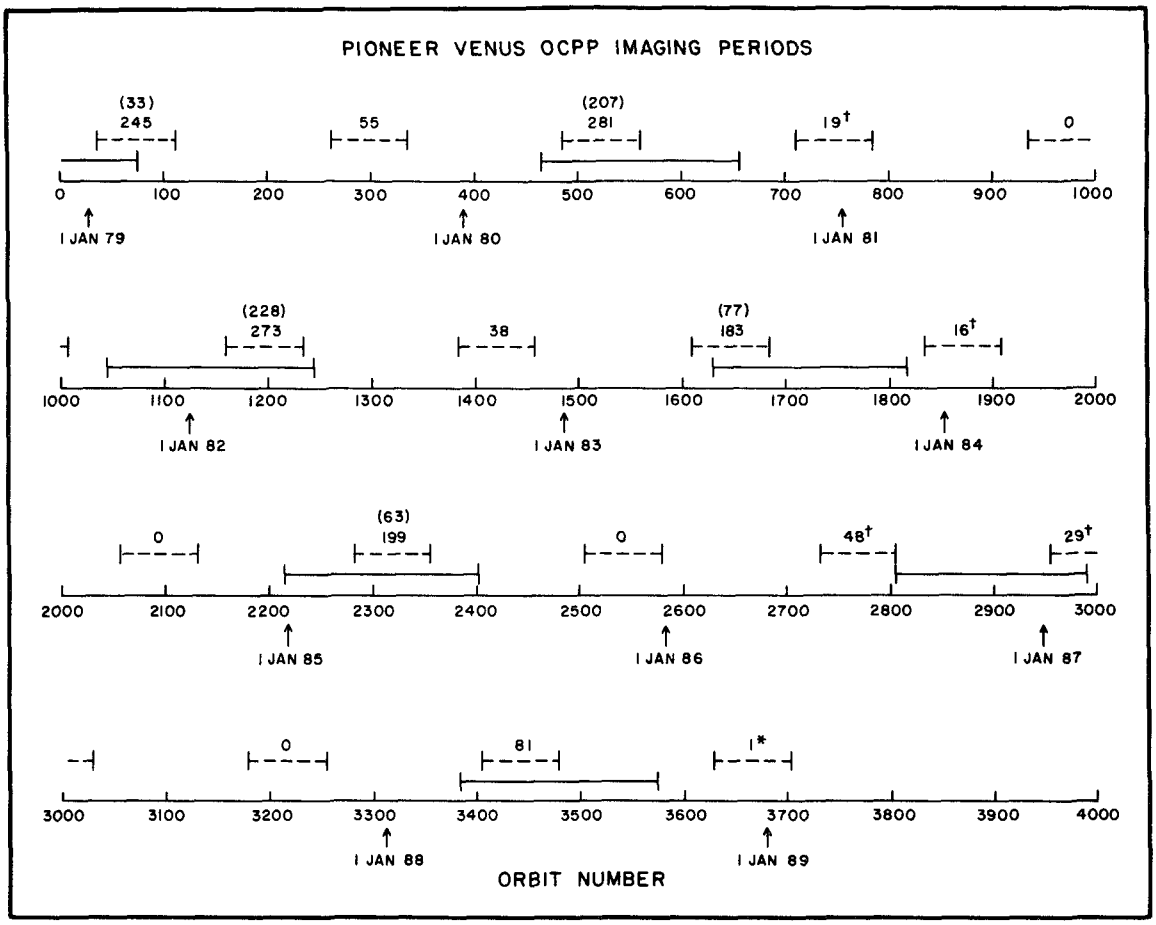

FIG. 1. Time history of Venus imaging opportunities showing the number of images collected at each opportunity and the number of image pairs tracked (in parentheses). (The number of pairs is more than half the number of images, since an image can be used in two pairs.) The dashed bars indicate time periods when the sunlit side of Venus is in view from the apoapsis portion of the orbit. The solid bars indicate time periods when the Earth–Venus distance was small enough to allow use of the smaller DSN antennas for high data rate telemetry; large antenna coverage is always possible, in principle, but was provided only for the nominal mission through late 1979. The 19 images collected in orbits 700–800 were obtained using a lower rate telemetry format that reduces the resolution of the images by about a factor of two. The single image obtained in late 1988, using the large antennas, was approved to provide publicity for the *Pioneer Venus* project.

obtain details of near-surface winds over the tropical ocean (Suchman and Martin 1976; Krishnamurti and Pasch 1982; Burpee and Reed 1982). Versions of this technique are now used operationally by several meteorological services to obtain routine windspeed measurements (e.g., Menzel et al. 1983; JMA 1984). The first planetary application of this technique was to the *Mariner 10* images of Venus (Suomi 1975; Limaye and Suomi 1981). Subsequent analyses of planetary imaging, including analysis of PV OCPP images (Limaye et al. 1982a; Limaye et al. 1988; Limaye 1988) and of *Voyager* images of Jupiter (Ingersoll et al. 1979, 1981; Beebe et al. 1980; Limaye et al. 1982b) and Saturn (Sromovsky et al. 1983), have all used a "manual" technique, where target selection in the first image and identification in the second image are performed by

TABLE 1. Image data statistics for each of the primary imaging epochs.

	1979	1980	1982	1983	1985
Total number images	245	281	273	183	199
Number days—one or more images	72	93	89	65	61
Total number image pairs	33	207	228	77	63
Number days—one or more pairs	23	93	89	44	40
Average number vectors per day	246	398	530	331	107

TABLE 2. Number of good wind vectors obtained in each latitude zone for each imaging epoch.

Center latitude	1979	1980	1982	1983	1985
−70	0	0	0	0	10
−66	0	1	5	6	4
−62	0	78	100	26	20
−58	0	290	410	98	61
−54	0	757	1038	179	128
−50	1	1339	1403	304	106
−46	17	1633	1603	434	133
−42	29	1743	1590	428	96
−38	257	1703	1493	407	101
−34	274	1667	1582	470	116
−30	252	1598	1620	465	124
−26	249	1045	1938	592	162
−22	278	1337	2191	670	216
−18	309	1447	2383	804	196
−14	298	1559	2505	754	226
−10	330	1573	2432	819	199
−6	338	1619	2541	818	174
−2	371	1610	2628	806	145
2	310	1692	2570	784	165
6	325	1620	2515	822	161
10	272	1485	2345	734	189
14	293	1375	2186	724	192
18	297	1228	1965	664	180
22	244	1138	1780	574	154
26	274	944	1558	445	132
30	237	1146	954	265	157
34	207	1107	807	255	161
38	146	1063	823	248	133
42	37	1079	776	242	120
46	14	937	711	264	125
50	1	766	446	209	102
54	1	360	186	122	48
58	0	66	65	73	22
62	0	10	1	29	16
66	0	1	0	10	0
70	0	0	0	2	0
Total	5661	37016	47150	14547	4264

a person visually inspecting the images. This manual technique is similar to that described by Menzel et al. (1983). We describe a fully automated procedure, similar to that employed operationally by the Japanese Meteorological Agency (JMA 1984), using the images in digital form for accomplishing the same task; an earlier version of this analysis method is described in Rossow et al. (1980).

The analysis method has five steps (Fig. 2): image navigation and mapping, high-pass contrast filtering of image brightnesses, target selection, search and displacement measurement. The images are represented by numerical arrays, where the array coordinates are positions on the planet and the numerical values represent the measured UV radiance or "brightness." Image navigation is the process of determining the planetary coordinates of each image element (pixel) in latitude–longitude and reprojecting it into a standard latitude–longitude mapping.

In the early analysis of these data, the original image brightness values were used without the high-pass filter step. Subsequent studies showed that better success was obtained at higher latitudes by using a high-pass filter to eliminate the larger scale brightness gradients; tracking of high-pass filtered images did not change the results at lower latitudes. All results from latitudes $\geq 30°$ were redone using the filtered images. Since target selection is systematic, the same targets were used in both versions; any vectors with large differences between the two measurements were rejected. The 1985 dataset was produced entirely with the high-pass filtering step.

Target selection is a systematic and complete sample of the first of a pair of images, without regard to the presence of specific "features". That is, some of the targets selected may have no cloud features present. Here, "target" refers to a numerical subarray representing some portion of an image.

Search refers to the procedure to find the same feature in the second of a pair of images. Essentially, this identification is associated with a maximum in the correlation of two numerical arrays, representing a sample of the spatial variations of UV brightness in the two images. Once the position of the maximum correlation is found, the displacement of the feature is measured by the distance between the centers of the two image portions.

b. Image navigation and remapping

An image pixel is located with respect to the surface of Venus by determining, at the time of the pixel sample, the position and motion of the spacecraft (supplied daily from DSN tracking), the position and orientation of Venus and the direction of instrument view. The position and orientation of Venus are calculated in celestial coordinates using the 1970 IAU definition of the rotation pole orientation[1] (right ascension = 273.0° and declination = 66.0°) and a rotation period of 243.0 days. Spacecraft attitude information and the position of the OCPP telescope with respect to the spacecraft are provided in engineering telemetry. The attitude information is only accurate to about 0.5° (equivalent to position errors up to about 600 km). Therefore, the predicted and observed portions of the bright limb of Venus are compared to refine the navigation: the precision of this fit is about one pixel (Travis 1979).

Once each image pixel is labeled by latitude–longitude coordinates, it is remapped into a standard map grid with 0.25° resolution in latitude and longitude. This mapping is done as a "backwards" procedure, where the closest image pixel coordinate is found for each map cell. This insures that all positions in the mapped image are filled. Since the map resolution is approximately the same as that of the original images near the subsatellite point, map cells at positions near

[1] This definition was changed in 1982 to right ascension = 272.8° and declination = 67.2°, with the same rotation period.

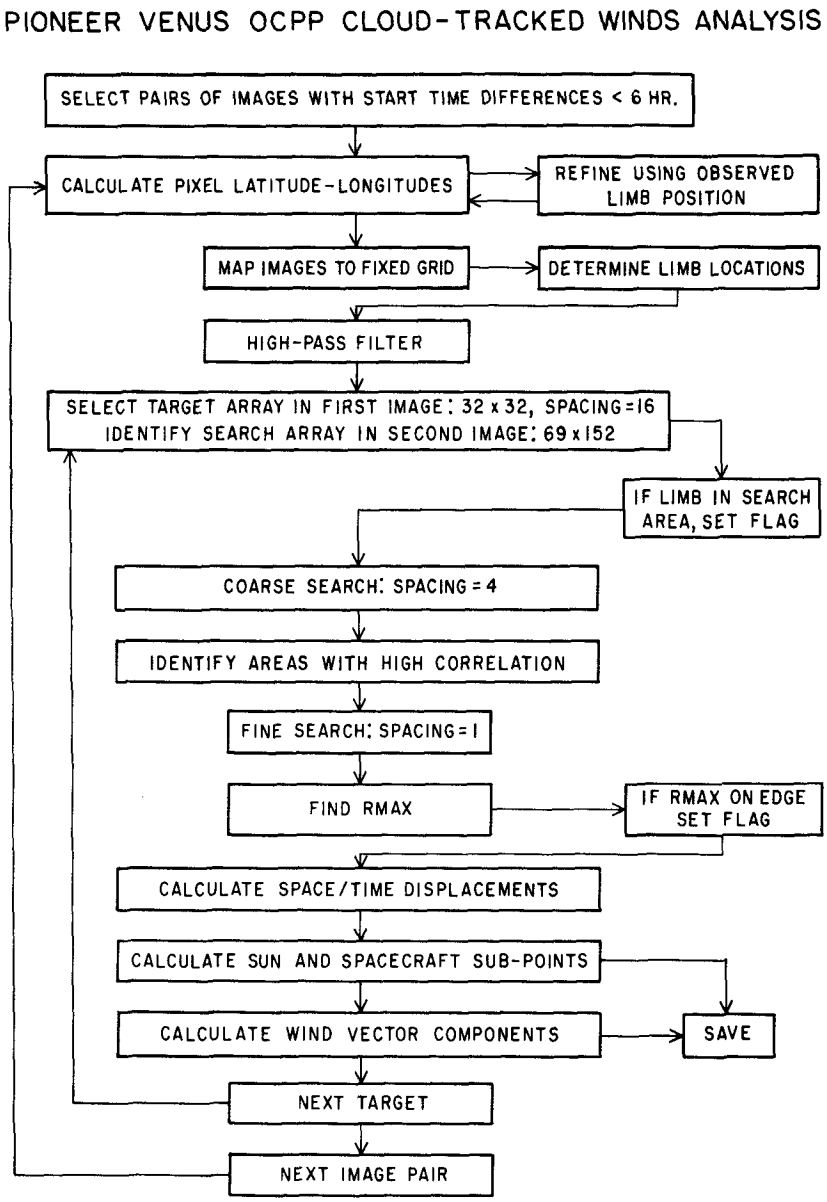

FIG. 2. Schematic of *Pioneer Venus* OCPP cloud-tracked winds analysis procedure.

the limb are filled by replication of the original image data, because of the lower resolution there.

c. *Image brightness contrast filtering*

The brightness contrast of the smaller features being tracked is enhanced by removing all larger scale brightness variations. This procedure simply subtracts from the original image the average brightness for each target area and adds an offset (mean image brightness) to avoid negative values near the terminator and limbs. This procedure removes both scattering geometry effects and the intrinsic large-scale UV brightness variations analyzed by DR90; only the smaller scale (within target) brightness variations are retained.

d. *Target selection*

Target selection in most early cloud-tracking procedures was done by visual inspection of the images to locate "distinct" features. This procedure is relatively easy to understand, since the human eye–brain combination is very good at pattern recognition; but it is difficult to quantify the selection criteria used and the uncertainties of feature identification. This procedure is also relatively time consuming. In developing our

automated scheme, we compared results with those from a fully manual scheme and hybrid schemes that combine some manual tasks with some automated calculations for the first imaging opportunity in 1979 (Rossow et al. 1980); later refinements in the automated analysis have improved the agreement (see section 4 and Limaye et al. 1988).

The approach adopted is essentially statistical, in that no attempt is actually made to "select" specific cloud features; rather, the first image in a pair is systematically sampled and all locations are considered to be valid targets (suggested by Travis 1978). Targets are defined by image pixel arrays of 32 × 32 (approximately 850 × 850 km), separated by 16 pixels; i.e., there is 50% overlap between adjacent targets in each dimension. Spatial autocorrelations calculated for 10 images from 1980 and 1982 fall below 0.5 at separations of 8–12 pixels (about 200–300 km); however, at higher latitudes this occurs for separations of 16–32 pixels in the east–west direction. Since we require a correlation ≥ 0.5 for all vectors retained in the dataset, each target can be considered to be statistically independent of its nearest neighbors.

Because the cloud features on Venus are much more "diffuse" than for Earth, manual target selection produces only about 50 motion vector measurements per image pair, with a strong concentration at low solar and satellite zenith angles (equivalent to low latitudes) where the feature contrast is higher (Rossow et al. 1980; Limaye et al. 1988). Using the digitial approach, correlations > 0.5 are obtained about 70% of the time, indicating the absence of distinct features in less than a third of the selected targets; additional criteria reject another 15%–25% of the results. Thus, the systematic sampling provides about 150 good results per image pair (Table 1) and a more uniform distribution of measurements with latitude (Table 2). Although this difference in the number of vectors obtained is not crucial to the precision of the average wind components, it is crucial to the detection of wave motions which requires examination of much smaller subsets of the data.

e. Correlation search

An area of the second image is searched to find the maximum correlation of the two 32 × 32 arrays representing the target and a portion of the search area; the target is assumed to be identified in the second image by a sufficiently large maximum correlation coefficient.

The search region in the second image is defined by an array of 69 × 152 pixels (1800 km north–south by 4000 km east–west), starting at the original location of the target in the first image. This search region encompasses meridional windspeeds of approximately 60 m s^{-1} in either direction and zonal windspeeds of approximately 15–250 m s^{-1} retrograde near the equator and 10–150 m s^{-1} at 50° latitude (the lower limit is set by eliminating cases where the maximum correlation occurs on the edge of the search region). Larger search regions were employed in the analysis of the first imaging period; these results show (see also section 4) that the actual range of measured values obtained is between ±25 m s^{-1} for the meridional and 60–130 m s^{-1} for the zonal windspeeds.

To save computation time, the search is conducted at two resolutions: a "coarse" comparison at every fourth map position (every 1° in latitude and longitude) in two dimensions and a "fine" comparison at every map position for all subregions with correlations above 0.95 times the maximum value from the coarse search.

The correlation coefficient between two numerical matrices, T and S, is calculated using

$$R(T, S) = \{[\Sigma_i \Sigma_j (T_{ij} * S_{ij})] - [\Sigma_i \Sigma_j T_{ij}] * [\Sigma_i \Sigma_j S_{ij}]/1024\}/[1024 * \sigma_T * \sigma_S] \quad (1)$$

where σ_T and σ_S are the standard deviations of the values in the matrices (we ignore the difference between 1023 and 1024 in the calculation of the standard deviation). With 1024 values in each matrix, the formal precision of the correlation coefficient is 3% and a correlation ≥ 0.5 is statistically significant.

Limaye et al. (1982) use a similar correlation calculation to refine the location of the cloud feature in the second image; however, the operator selects a small subregion of the second image for the correlation search. Our procedure is fully automatic.

f. Displacement measurement and windspeed calculation

The target displacement is measured as the distance in planetary coordinates between the centers of the target array and the subarray in the search region with the maximum correlation. Total displacements in latitude and longitude are converted to zonal and meridional distances using the radius of Venus at cloud level (6120 km). The time between images is refined to determine the time at which the particular pixels in each image were actually observed. Displacement distances divided by the time differences give the zonal and meridional windspeeds. The location is the average of the positions in the first and second image.

g. Final data selection

Several studies were conducted to determine the quality of the feature identifications and to select criteria for acceptance of measurements (see section 4). Based on the test results and an examination of the distribution of all wind measurements for all imaging periods, only those wind measurements with *RMAX* ≥ 0.5 and zonal windspeeds from 65 to 125 m s^{-1} are accepted.

4. Error assessment

a. Displacement precision and navigation errors

With a four hour separation between PV images, a 2 m s^{-1} windspeed produces a displacement of about 30 km, about the size of an image pixel near the center of the image; at higher latitudes or near the limb, one pixel is equivalent to about 4 m s^{-1}. In other words, the intrinsic precision of the windspeed measurements due to the spatial resolution of the images is about 2–4 m s^{-1}.

Navigation errors affect the wind measurements in two ways: translation errors affect the conversion of the cloud feature displacements into physical distances, and rotation errors affect the division of the displacement vector into the zonal and meridional wind components. The latter error is most important for the meridional wind component, since the zonal wind component is almost two orders of magnitude larger than the meridional.

Translation uncertainty in the pixel navigation is estimated by the precision of determining the limb position at one place which is about one pixel (Travis 1979); for the difference in positions between two images, the uncertainty is 1–2 pixels. However, since the fit to the limb position is performed at all illuminated locations around the perimeter of the imaged planet, we adopt one pixel as an upper limit. This implies a windspeed error of about 1–2 m s^{-1}.

We can estimate a range for the rotation effect from the estimated angular error of the spacecraft attitude from the star tracker information (0.5°) and from half of the full tilt of Venus relative to the ecliptic (3°); these angular errors are equivalent to errors in the meridional wind of about 1–3 m s^{-1} for a zonal windspeed of 90 m s^{-1}.

b. Cloud shape effects and changes

Terrestrial experience tracking clouds shows that the size of cloud features must be smaller than wavelengths of the predominant propagating waves but larger than convective scales to represent bulk windspeeds accurately (Fujita et al. 1975; Hasler et al. 1977; Wylie and Hinton 1981). Power spectra of cloud features in Venus images show that the dominant length scales are >1000 km (Rossow et al. 1980; Del Genio and Rossow 1982). *Mariner 10* high resolution images show few features smaller than 20–30 km; "convective" features appear to be ~100 km (Belton et al. 1976a). We track features with sizes of 200–600 km. The image time separation selected for OCPP represents a compromise between two accuracy considerations, based on studies of the higher time and space resolution *Mariner 10* images (Travis 1978): minimizing cloud shape changes by minimizing the time separation and maximizing cloud displacements by maximizing the time separation.

Radical changes in cloud shape decrease the correlation between the two images to a value below our acceptance threshold. Smaller changes in cloud shape cause errors in the displacement that are less than the feature size by changing the "apparent" center of the feature. We estimate this effect from the rate of variation of the correlation coefficient near the peak value (Fig. 3). Figures 3a,b, and c show cases with relatively high, moderate, and low peak correlation values, respectively. The first two presumably represent well-defined, relatively constant features, while the latter may be diffuse and/or changing. The rate of decrease of correlation with distance in these figures suggests that the error due to a shift of the feature center is no more than 10%–15% of the target size, equivalent to about 6–9 m s^{-1}. A synthetic test of the correlation sensitivity supports this estimate: correlating an image to itself with added noise (10% contrast) in the second image changes the windspeed values by only a few m s^{-1}.

If the cloud feature has a significant constant (Fig. 3d) or periodic (Fig. 3e) structure, the location may be nearly indeterminate. On Venus, clouds at higher latitudes tend toward "streak-like" features with small scale, quasi-periodic patterns (Belton et al. 1976b; Rossow et al. 1980; Del Genio and Rossow 1982). This sometimes produces multiple correlation maxima (Fig. 3f). These cases are, however, also associated with reduced *RMAX* values (Fig. 4) and sensitivity to very small changes in the precision of the calculations. At values of $RMAX > 0.7$, the majority of the vectors have single maxima.

c. Statistical tests

Histograms (Fig. 5) of the frequency of occurrence of zonal windspeeds with no selection criteria applied show a distribution with three different populations: a nearly uniform distribution over all possible values (called the "uniform" group), a collection of very low values between 15 and 45 m s^{-1} (called the "slow" group), and a collection of values between 65 and 125 m s^{-1} (called the "main" group). The meridional windspeed distribution associated with each zonal windspeed value is shown in Fig. 6. The "slow" group is sometimes bimodal in zonal windspeed and is always trimodal in meridional windspeed. The "uniform" group population decreases linearly with increasing zonal windspeed, but is also trimodal in meridional windspeed. The zonal/meridional windspeed ratios for both these groups are also much smaller than for the "main" group. The main group exhibits a roughly Gaussian shape in both the zonal and meridional windspeed distributions. In this section, we show evidence that these groups are actually distinct in their behavior, that two of these populations are caused by specific problems with the tracking analysis, and that the values from 65–125 m s^{-1} represent the actual winds.

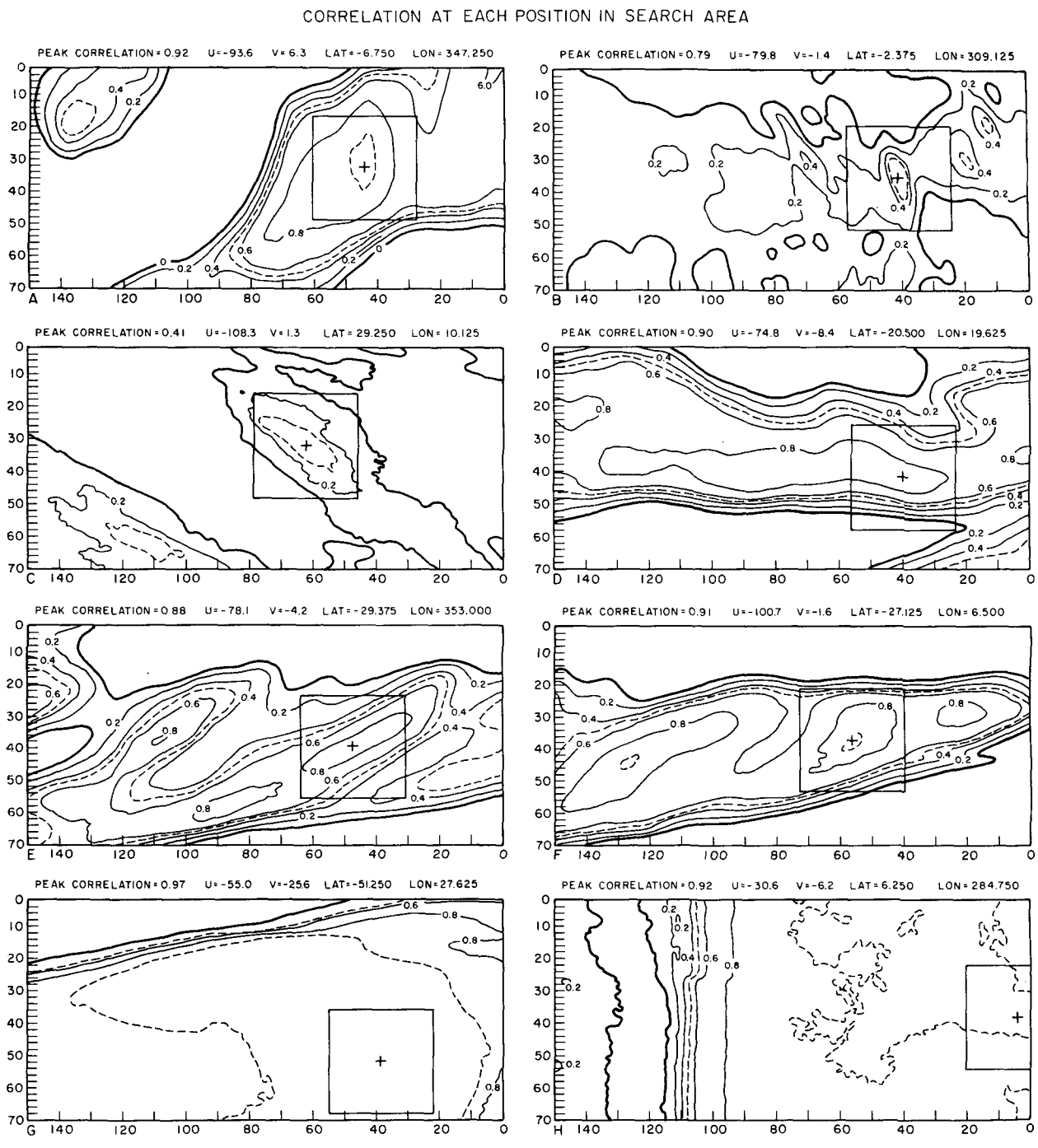

FIG. 3. Examples of the distribution of correlation coefficients over a search area: (a) single, isolated, high peak correlation, (b) single, high contrast peak with moderate correlation, (c) single peak with low correlation, (d) single peak within ambiguous feature, (e) quasi-periodic feature, (f) multiple correlation peaks associated with midlatitude streaks, (g) uniform, high correlation caused by low image resolution at high latitudes, and (h) uniform, high correlation caused by large brightness gradient near limb. The square indicates the size of the target area; the cross indicates the location of the peak correlation. The blank regions are areas of small (> -0.3) negative correlations.

Vectors in the uniform group represent about 25% of the total and differ from the other two groups in all or some of three ways: (1) the distribution of correlation coefficients over the search area usually has two or more broad maxima with roughly equal magnitudes (e.g., Figs. 3d, 3e, 3f and 7), (2) the peak values of *RMAX* are generally lower than for the other two groups, typically <0.6 (Figs. 4 and 7), and (3) these vectors exhibit great sensitivity to any changes in the precision of the calculation of the correlation coeffi-

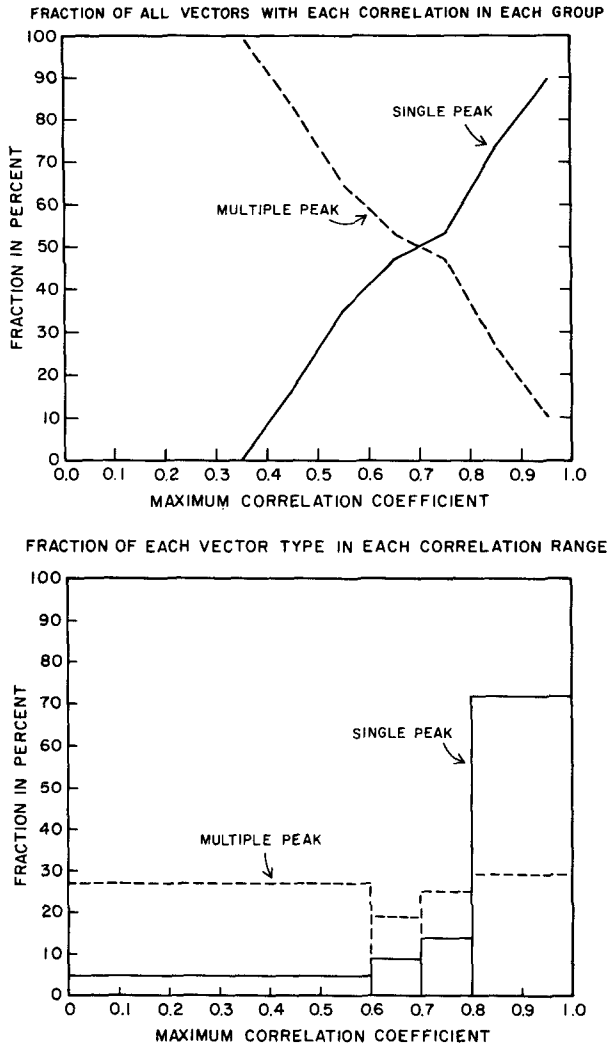

FIG. 4. Distribution of maximum correlation values (*RMAX*) for two types of correlation patterns (solid—single peak; dashed—multiple peak).

cients, because the peak correlations of the multiple maxima are so similar (Figs. 3d,e, and f). An example of the latter effect is the changes caused by high-pass filtering the images: most of the zonal windspeeds were reduced and the trimodal meridional windspeed distribution was nearly eliminated. The relative number of these "ambiguous" cases increases with latitude (Fig. 5) because cloud features are more elongated and "wavelike" in middle latitudes.

The slow group is about 20% of the total and is caused by decreased resolution near the limbs (Fig. 3g) and/or by strong gradients in image brightness near the limbs and terminator (Fig. 3h). This group (and the uniform group) is concentrated at larger distances from the subsatellite and subsolar points (Fig. 8). The relative proportion of wind vectors in the slow group grows at higher latitudes (Fig. 5), where both effects occur. The slow group vectors also differ from the other two groups by being almost entirely composed of measurements with $RMAX \geq 0.8$ (Fig. 7). For these vectors there is either no distinct correlation peak or only one very broad peak (Figs. 3g,h).

The characteristics of the slow group vectors can be explained, in the case of strong illumination gradients, by the resemblance of one segment of the gradient to another and by the tendency of the correlation to locate the same mean brightness on the intensity gradient regardless of smaller brightness variations. When we repeat the tracking for the same targets after high-pass filtering the images to eliminate intensity gradients, almost all low speed vectors are eliminated at low latitudes, whereas the main and uniform groups are not changed (Fig. 9). The remaining population of slow values is equal to the linear extrapolation of the uniform group to low zonal windspeeds. Since the multiple correlation peak cases often have peaks at low, medium, and high zonal windspeeds (e.g., Fig. 3f), we interpret this residual slow group to be part of the uniform population.

The explanation, in the case of low resolution, is that the repetition of brightness values in the projection of the data into a constant latitude–longitude grid reduces the importance of the smaller brightness variations and increases the correlation coefficient. This explains why fewer vectors are eliminated by high-pass filtering at high latitudes where the resolution effect is strongest (Fig. 9).

High-pass filtering increases the zonal windspeed inferred for those targets that gave low zonal windspeeds with unfiltered images and eliminates most of the spuriously large meridional speeds, characteristic of this group. The successful reduction of the slow group population and the movement of both slow and uniform group vectors into the main distribution by high-pass filtering led to the reprocessing of all the data at higher latitudes using this technique.

The main group contrasts with the other two populations in that it is characterized by (1) a unimodal distribution of meridional windspeeds (Fig. 6), (2) single correlation peaks (Fig. 7), (3) maximum correlations from 0.8 to 0.9 (Fig. 7), (4) insensitivity to the precision of the correlation calculations, (5) more uniform distribution in distance from the subspacecraft and subsolar points (Fig. 8) and (6) being unchanged by high-pass filtering of the image brightness values. These characteristics, together with agreement of the zonal windspeeds obtained from these vectors with manual tracking results (see below), support the interpretation that the vectors in this group represent the actual winds on Venus.

d. Error summary

Combining (rms) all the direct sources of error (displacement precision = 2–4 m s^{-1}, navigation = 2 m

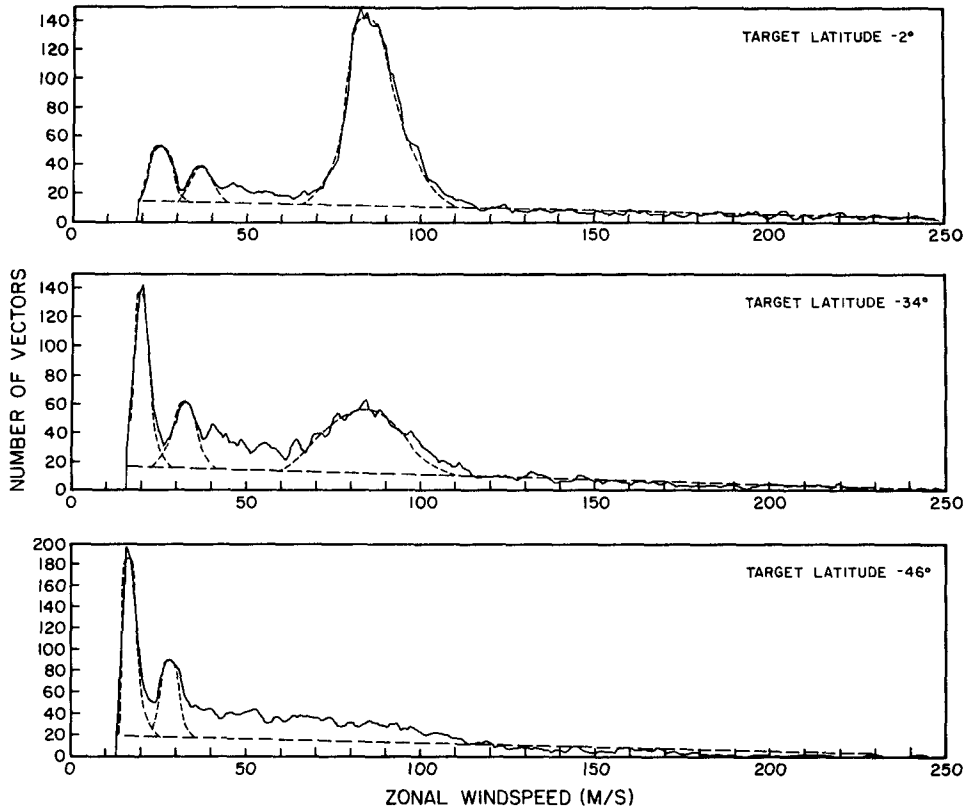

FIG. 5. Distribution of all zonal windspeed measurements from the 1982 imaging period in increments of 1 m s^{-1} (a) near the equator (−2°), (b) at −34° and (c) at −46° latitude. No result is excluded. Dashed lines illustrate fits of Gaussian distribution shapes to the slower and medium speed components and a straight-line fit to the "uniform" vector population. Note changes of vertical scales.

s^{-1}, coordinate rotation = 1–3 m s^{-1}, shape changes = 6–9 m s^{-1}), assumed to be uncorrelated, gives a formal estimate of the error of 3–5 m s^{-1} for a single measurement at low latitudes, increasing to about 6–10 m s^{-1} at 60°. Much larger errors can occur because of the absence of an actual cloud feature, because of ambiguous or quasi-periodic cloud features, and because of intensity gradients. If the data are restricted to have correlations $RMAX \geq 0.5$ and to be in the main group (zonal windspeed, $65 \leq u \leq 125$ m s^{-1}), this eliminates most of the vectors influenced by the larger sources of error.

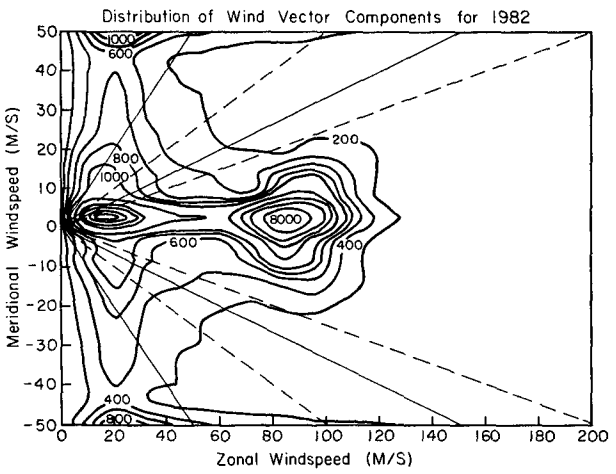

FIG. 6. Distribution of all meridional windspeed measurements from the 1982 imaging period as a function of the corresponding zonal windspeed. The solid and dashed straight lines indicate constant integer values of u/v.

An upper limit on the total measurement error of the remaining wind vectors is set by the smallest width distribution observed. The smallest widths (standard deviations) of the zonal wind distributions are about 10 m s^{-1} near the equator and about 12 m s^{-1} at higher latitudes. For meridional winds these values are about 13 m s^{-1} and 15 m s^{-1}, respectively; however, the bulk of the data form a somewhat narrower distribution with a small number of values far from the mean.

Since the estimated errors are only slightly smaller than the observed standard deviations of the windspeeds, we test whether the wind variations contain a contribution from real wind variations by examining the evolution of the standard deviations of time-averaged windspeeds as a function of the number of samples averaged. Figure 10 compares this evolution with that expected for random noise (namely the standard

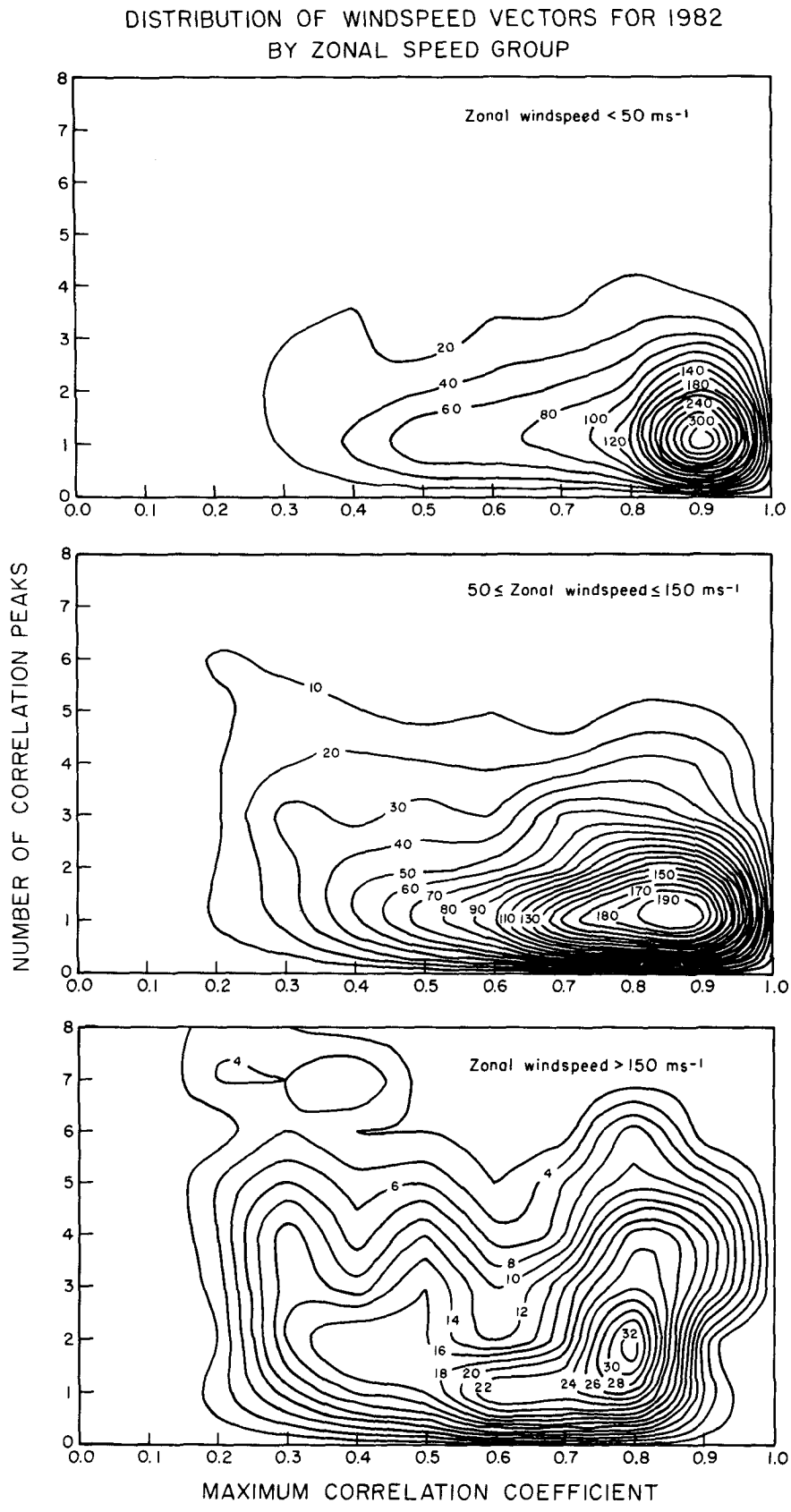

FIG. 7. Distribution of wind vectors as a function of the maximum correlation value and the number of correlation peaks in the search area in three ranges of zonal windspeed: (top) "slow speed" vectors ($u < 50$ m s^{-1}), (middle) "medium speed" vectors ($50 \leq u \leq 150$ m s^{-1}), and (bottom) "fast speed" vectors ($u > 150$ m s^{-1}).

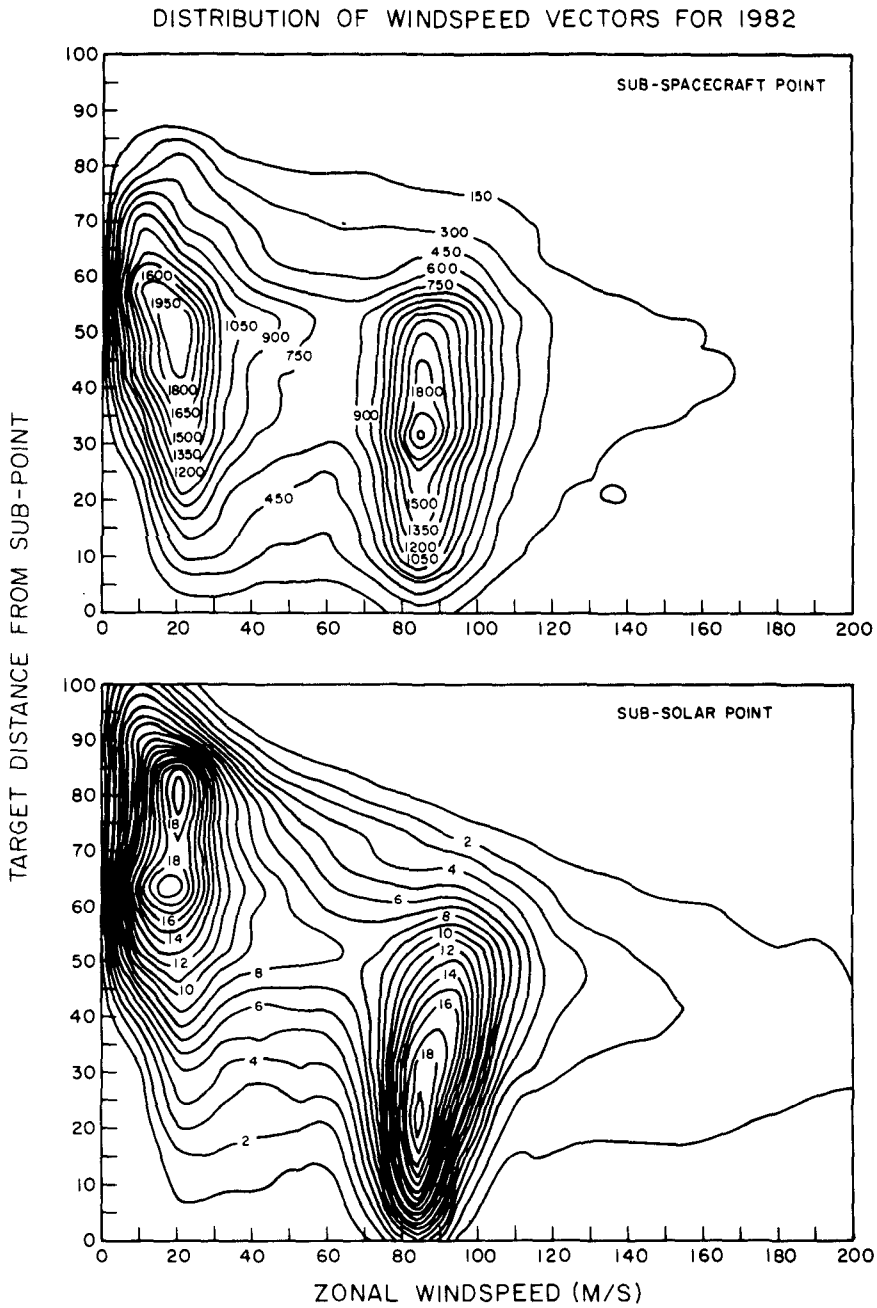

FIG. 8. Distribution of wind vectors as function of zonal windspeed and distance from the (a) subspacecraft point and (b) subsolar point. Distance is indicated as a percentage of the distance to the geometric limb of the planet.

deviation of the averages decreases inversely as $\sqrt{N}$). At lower latitudes, the data do not follow the evolution expected for random error. At higher latitudes in 1982 the results are consistent with random behavior, however, the behavior deviates from random in 1980. The fact that the evolution changes from 1980 to 1982, corresponding to the disappearance in 1982 of almost all other evidence for waves (see section 5, Table 7 and the discussion in DR90), suggests that the measured windspeed variations at high latitudes are not totally due to measurement errors, except in 1982. This conclusion is reinforced by the fact that the standard deviations vary between epochs (Table 7) in ways that are not proportional to differences in the number of vectors obtained.

We adopt as a conservative estimate of the error in a single measurement, for both the zonal and meridional windspeed components, 10 m s^{-1} at the equator

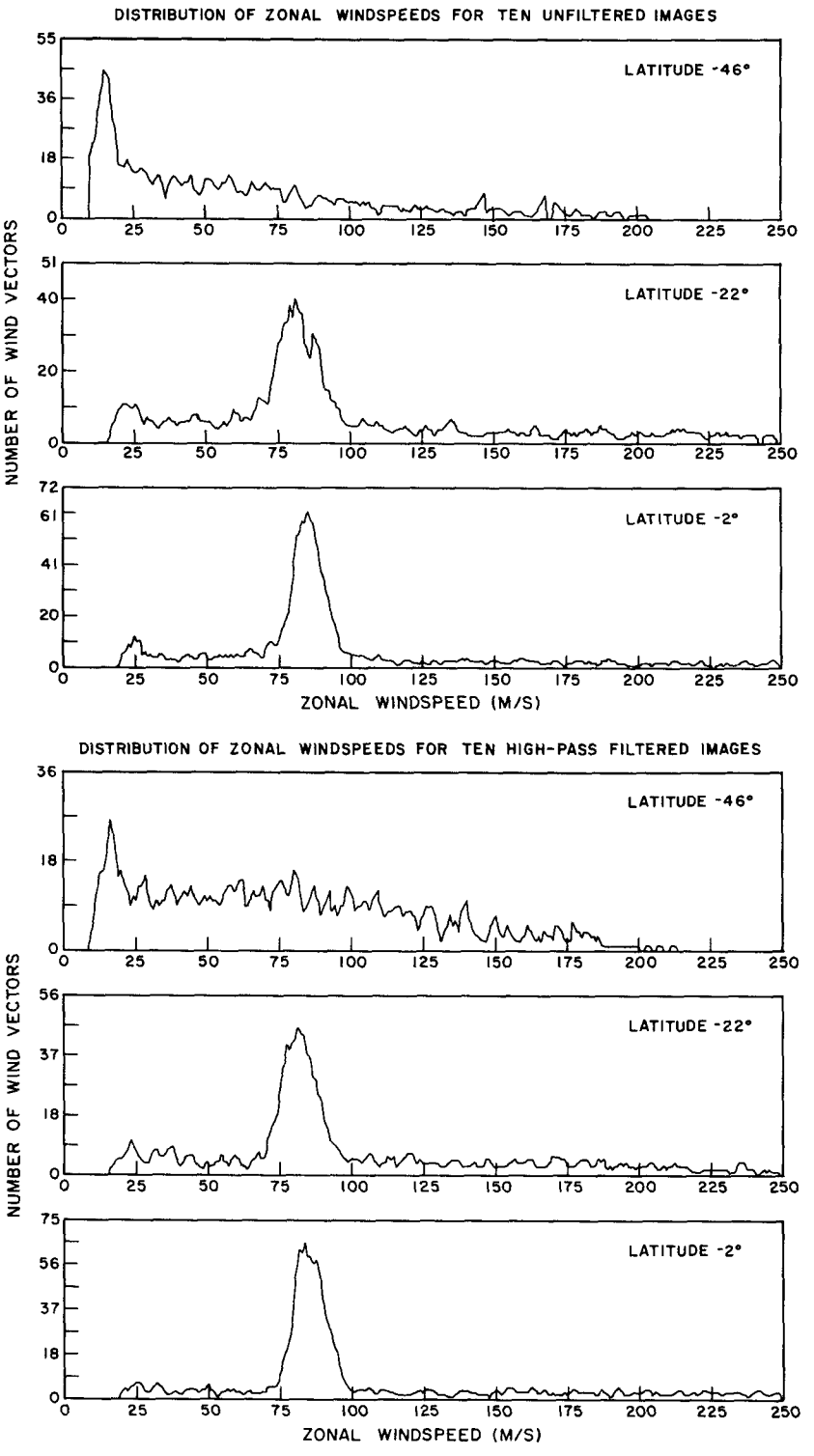

FIG. 9. Distributions of zonal windspeeds in three latitude zones measured for the same ten image pairs (a) without high-pass filtering of the brightness values and (b) with high-pass filtering. Note changes of vertical scales.

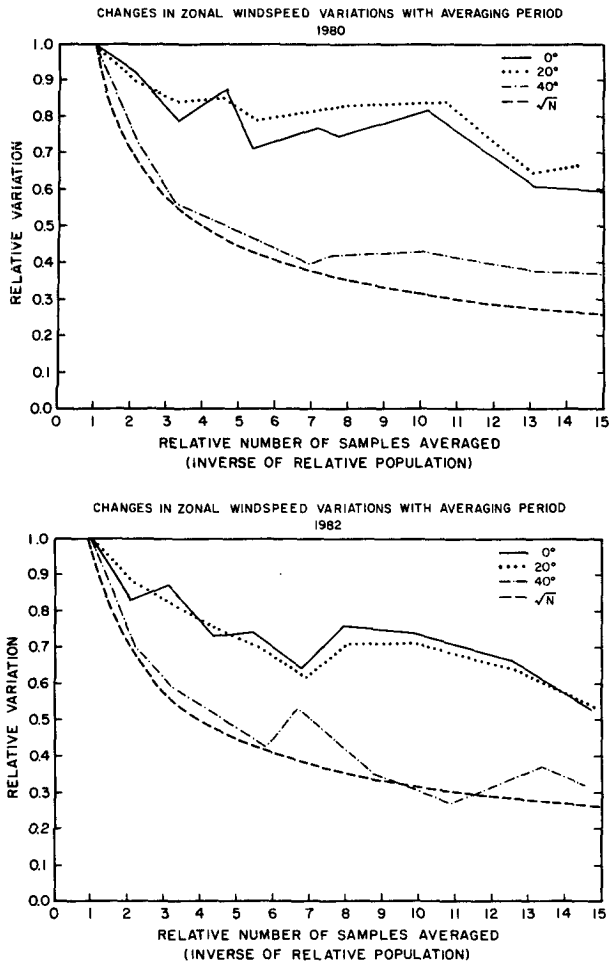

FIG. 10. Evolution of the standard deviation of average zonal windspeeds in a time series as a function of the number of samples averaged (or equivalently, the number of days averaged), calculated using the daily mean values in three latitude zones for (a) 1980 and (b) 1982. The dashed curve shows the expected evolution of the standard deviation if the time variations are due solely to Gaussian-distributed noise, which is inversely proportional to $\sqrt{N}$, where N is the number of days averaged.

increasing linearly to 20 m s^{-1} at ±60° latitude. Since the shape of the main group distribution is quasi-Gaussian (Fig. 5), the accuracy of an *average* windspeed will increase like the square root of the number of observations included in the average (Fig. 10 shows this behavior in one case where we have other evidence for the absence of wave activities). Thus, the error in the mean windspeed is <2–3 m s^{-1}, if the number of measurements is >50. This formal estimate does not, however, account for other problems in interpretation of the results that are discussed below.

e. *Determining mean windspeeds*

The limiting zonal windspeed values used to edit the final data were selected to include the range of zonal windspeeds at which the number of wind vectors exceeds the extrapolated background population associated with the "uniform" group and to encompass the range of variation of the "main" group with latitude and between imaging periods. These limits are also always more than one standard deviation away from the peak value in the main group at each latitude. A similar analysis was performed for all imaging periods and latitudes; a single set of cut-off values was used only because it included all of the main group values.

The use of these cut-offs introduces an additional, nonrandom source of error in mean windspeeds. Table 3 shows the effects of varying these cut-off values by 10 m s^{-1}, both together and separately. Because there are more spurious vectors on the slow side of the main group, changes in the lower cut-off cause larger differences in the mean value than changes in the upper cut-off; thus, widening the filter decreases the mean value but narrowing the filter has little effect. Shifting the filter window location (which is the same as changing the mean wind speed in the opposite sense), causes changes in the mean value of the same sign; hence, keeping the filter location fixed *underestimates* changes in windspeed. The dependence of the mean windspeed on filter location (Table 3 shows the worst case) is a significant source of uncertainty poleward of about 40° latitude, where we cannot identify the lower limit of the main group, even after high-pass filtering (Fig. 9). We, therefore, view the mean windspeeds at these latitudes as containing information only on relative differences between different hemispheres or epochs and then only when these differences are dramatic.

We emphasize that we examined all distributions before picking filter limits to be sure that no distribution

TABLE 3. Sensitivity of average zonal windspeeds to cut-off values used to edit the dataset. Standard cut-off values are 65 and 125 m s^{-1}. The results are shown for two latitude zones for 1982. The meridional windspeed is not very sensitive to the cut-off values, except when the number of vectors is low.

Latitude range	Lower limit ±10	Upper limit ±10	Upper/lower limits +10	Upper/lower limits −10	Upper/lower limits +10/−10	Upper/lower limits −10/+10
0–20	±2.5	±2.0	+3.5	−4.5	−2.0	+0.5
30–50	±5.5	±4.0	+6.5	−10.5	−5.0	+2.5

was very different in location. Variations with latitude and time of the windspeed values at which the main group population equals the estimated uniform group population (cf. dashed lines in Fig. 5), suggests uncertainties in the cutoff values of no more than 5 m s^{-1}, except at latitudes > 40°.[2] Table 3 indicates that the associated systematic errors are no more than 2 m s^{-1}.

A final consideration, that is not usually addressed for other data sets, is the effect on the averages caused by limited space/time samples of the OCPP. If the sample is too sparse to represent the whole distribution of windspeeds or represents a biased sample, then averages of the data will be biased estimates of the true average. Our measurements occur in the same solar season (the subsolar latitude moves from the Southern Hemisphere to the equator over an imaging period), do not cover all planetary longitudes and view specific planetary longitudes at similar solar positions. Calculation of the zonal mean and eddy wind components with an incomplete sample of wave phases can introduce errors at shorter time scales. Similar problems arise even for analysis of the terrestrial general circulation because of incomplete sampling of ocean regions and much of the Southern Hemisphere (Oort and Peixoto 1983).

To illustrate the effect of incomplete sampling, consider a steady zonal flow, $U(\theta)$, with a single propagating wave, wavenumber $k = 1$, amplitude $u'(\theta = 0) = 10$ m s^{-1} and phase speed $c = (15 \text{ m s}^{-1})/(r\cos\theta)$, where r is the radius of Venus at cloud top, 6120 km. At any moment the zonal windspeed at some latitude, θ, and longitude, λ, can be described by

$$u(\theta, \lambda, t) = U(\theta) + u'(\theta)*\sin(\lambda + c*t) \quad (2)$$

where $\lambda + c*t$ is the longitudinal phase of the wave at time, t. With measurements covering all longitudes, the mean zonal flow is easily found by

$$[u(\theta, t)] = \int_0^{2\pi} \{u(\theta, \lambda, t)*d\lambda\}/(2\pi) = U(\theta). \quad (3)$$

If we obtain measurements only over 100° of longitude (1.74 radians), for example, and at different times, then the only quantities that we can calculate are

$$\langle u(\theta, t)\rangle = \int_0^{1.74} \{u(\theta, \lambda, t)*d\lambda\}/(1.74)$$
$$= U(\theta) + \{u'(\theta)/(1.74)\}* \{1.17*\cos(c*t) + 0.98*\sin(c*t)\}, \quad (4)$$

which varies with time, and

$$\langle\langle u\rangle\rangle = \int_0^T \int_0^{1.74} \{u(\theta, \lambda, t)*d\lambda*dt\}/1.74/T$$
$$= U(\theta) + \{u'(\theta)/(1.74)\}*\{1.17*\sin(c*T) - 0.98*\cos(c*T) + 0.98\}/(c*T). \quad (5)$$

The second bracketed factor in (5) goes to zero only if the time average covers a long enough period that all longitudinal positions of the wave are included; i.e., $c*T = 2\pi$. Moving with the mean flow, this period is just the time required for the wave to propagate once around the planet relative to the mean flow, about 30 days (see DR90); however, as we observe Venus, the mean flow carries a transient wave around the planet in about five days. [Note that the *Mariner 10* wind measurements only spanned a three day period (Limaye and Suomi 1981)]. Thus, if the wave amplitude is constant, $\langle\langle u\rangle\rangle$ converges to the true zonal mean speed after averaging the observations over a period of approximately five days. Note, also, that in this simple case the value of $\langle\langle u\rangle\rangle$ will oscillate about U with decreasing amplitude as T is increased.

With a mixture of wave phases and wavelengths, the behavior of $\langle\langle u\rangle\rangle$ with changing T will be much more complex. As determined in Del Genio and Rossow (1982, 1990), the dominant wave motions occur at planetary scale (wavenumbers < 3–5) and the phase speeds of the lowest wavenumber waves are estimated to be about 10–30 m s^{-1}. To remove all transient wave contributions to the average windspeeds, we must average over at least a time period that allows all the waves to propagate once around relative to the mean flow and relative to each other. For Venus, this time period is at least 30–40 days. Such a contamination of the "zonal mean" windspeeds by waves may explain the different latitudinal distribution obtained from the *Mariner 10* observations[3] (Belton et al. 1976b); however, time variations in the mean zonal flow cannot be ruled out (see section 5).

To test whether we have eliminated the effects of transient waves, we composite the data in coordinate frames rotating with a 4-day period, with a 5-day period, and with a 20-day period, corresponding to the two periodicities detected in the image brightness variations and their beat period. Table 4 compares the resulting zonal mean windspeeds. The differences can be as much as 1 m s^{-1} for the shorter image sequences. If the zonal mean flow and wave amplitudes also vary on time scales less than 30–40 days, then $\langle\langle u\rangle\rangle$ includes a complex mixture of wave phases and these

[2] At higher latitudes the "shoulder" in the windspeed distribution near 100–120 m s^{-1} (Fig. 5) does not shift out of this range of values in any epoch.

[3] For example, if we take the same wave parameters as above and assume that for *Mariner 10* the effective longitude coverage is about $c*T = 3(2\pi)/5 = 216°$, then $\langle\langle u\rangle\rangle - U \approx 2$–5 m s^{-1}.

additional time variations as well. We cannot distinguish short-term amplitude variations from propagating waves. However, we can resolve the larger scale (time and space) wave motions that persist over the averaging time period.

If there are also waves present with phases that are correlated with the observations, then their effect cannot be removed completely from an incomplete sample of (relative) longitudes. Measuring UV cloud feature motions limits results to the sunlit longitudes of Venus; hence, our measurements contain an incomplete longitudinal sample of any solar thermal tides, which appear as "standing" waves in our results. The apparent amplitude of the solar wave in our results is as large as 10–15 m s^{-1} (see section 5). The particular phase and wavenumber of this wave, together with the (relative) longitude coverage we have, suggests that the bias in the average zonal windspeeds is probably no more than $\approx$2 m s^{-1}; the bias in the meridional windspeed may be larger.

An additional bias can be created by a nonuniform distribution of observations with respect to such a standing wave. Table 4 shows the magnitude of this effect by comparing the usual longitudinal average of our data with the average performed in fixed solar coordinates; the effect is only about 1–2 m s^{-1}. In subsequent analyses, we use the zonal mean values obtained in solar fixed coordinates to eliminate most of the tidal effect.

In summary, we estimate the uncertainty in average zonal and meridional windspeeds to be about 1 m s^{-1} at the equator and 2 m s^{-1} at 40° latitude; uncertainties at higher latitudes are larger and difficult to estimate.

f. Comparison to manual tracking results

Another assessment of the accuracy of the wind measurements, particularly systematic errors, is obtained from a comparison to a completely independent set of measurements using the same data. Limaye et al. (1988) have presented such a comparison for 1979 and 1982. The comparisons for 1982 include results from two independent manual tracking datasets and from our new digital tracking results; they estimate the *differences* in average zonal windspeeds to be less than 2 m s^{-1}, when the number of vectors in the average is >50. Figure 11 shows a similar comparison for 1979, including the old digital tracking results from Rossow et al. (1980). Editing the digital vectors to isolate the main group clearly improves the agreement in 1979; in the latitude range where there are sufficient vectors from the manual tracking (±20°), the agreement of the average values is within ±1 m s^{-1}. This result is consistent with the predicted uncertainty estimated from single measurement errors and, more importantly, indicates that the editing procedure does not introduce any significant bias.

TABLE 4. Changes in mean zonal and meridional windspeeds caused by compositing the data in different rotating coordinate frames: 4-day, 5-day, 20-day and solar.

Imaging epoch	Range of differences in the 4/5/20-day composites		Rms differences between solar and regular averages	
	u (m s^{-1})	v (m s^{-1})	u (m s^{-1})	v (m s^{-1})
1979	1.2	2.1	1.0	1.6
1980	0.1	0.1	1.1	1.7
1982	0.1	0.1	0.8	1.5
1983	0.5	0.9	0.8	1.4
1985	1.0	2.0	1.2	1.6

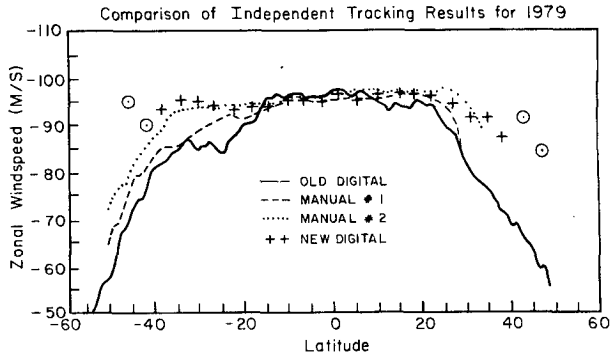

FIG. 11. Comparison of average zonal wind profiles for 1979 obtained from manual tracking of cloud features by two different people (see also Limaye et al. 1982; 1988) and from two versions of the digital tracking method. Circles are values from the new digital method at latitudes with less than 50 vectors.

g. Comparison to other wind measurements

Comparisons to the direct probe and balloon measurements can provide only consistency checks, since most of the probes did not make measurements in the altitude range of the cloud-tracked wind measurements. However, all of these measurements give windspeeds > 60–70 m s^{-1} with vertical shears $\approx$ 1–2 m s^{-1}/km (averaged over a scale height) at levels about 5–10 km below the cloud-tracked wind levels (see summaries in Schubert 1983; Kerzhanovich and Marov 1983; Limaye 1985). Limaye (1985) extrapolates probe measurements[4] to 65 km for some latitudes, producing values consistent with our results (Fig. 12). This consistency of in situ measurements with our measurements also precludes any very large phase speed effects. Moreover, the close agreement of the *Pioneer* Day and Night Probe up to 62 km (Counselman et al. 1980) supports our contention that the effects of the solar tides on our results are not very large.

[4] Most probe measurements begin slightly below this level.

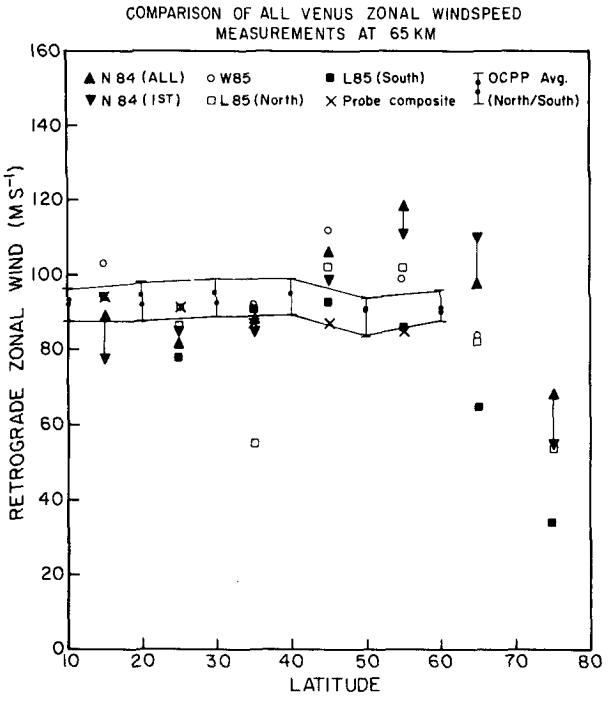

FIG. 12. Comparison of the latitudinal variation of the average OCPP zonal windspeed with that inferred from thermal structure measurements by the RSS at 65 km altitude (the estimated location of our measurements) and from a composite of entry probe measurements. Results from both hemispheres, where available, are shown together. The range of variation among OCPP imaging periods is also indicated by the vertical bars. N84: Newman et al. (1984); W85: Walterscheid et al. (1985); L85: Limaye (1985).

Other inferences of mean zonal windspeeds near cloud tops have been made from measurements of the mean thermal structure and the assumption of cyclostrophic balance. Limited thermal structure measurements have also been obtained from the entry probes (Seiff et al. 1980; Kerzhanovich and Marov 1983) and from the Orbiter Infrared Radiometer (Taylor et al. 1980); but radio occultation profiles are more extensive, covering more of the planet over longer time periods (Kliore and Patel 1980, 1982). The inferred mean zonal windspeed as a function of height and latitude has been reported from analysis of two subsets of these data (Newman et al. 1984; Walterscheid et al. 1985) and from a different analysis of the whole dataset (Limaye 1985).

There are several sources of error in inferring the zonal windspeed from the thermal structure (Rossow 1985). These errors arise, first, because the temperature structure is assembled from observations of different locations at different times. Since a long time period is required to obtain a global temperature field, time variations in the flow can introduce spurious latitudinal gradients that are not actually present in the mean. The radio occultation results include almost no observations between 15° and 30° latitude and the data on either side of this gap are from different hemispheres (Newman et al. 1984) or from different years (Walterscheid et al. 1985). Intercomparison of these different results indicates sensitivity to the precise selection of data, particularly at low latitudes. Second, the data are so sparse that interpolations and curve fitting are required to estimate derivatives; comparison of the results of Newman et al. (1984) and Walterscheid et al. (1985) with those of Limaye (1985), obtained by a different technique, illustrate significant sensitivity to the processing procedures. Third, since the relation between the mean temperature field and the mean zonal flow is nonlinear in cyclostrophic balance, errors arise because this kind of analysis mixes some contribution of eddy motions with the zonal flow. However, the inference of average zonal windspeeds is expected to be good to within 10%–20% of the windspeed, or about 10–20 m s^{-1}.

The comparison of the average of all our results with the probe and radio occultation results (Fig. 12) shows good agreement in both the magnitude and latitudinal distribution of the mean zonal windspeed. (Note that the precise determinations of height are not likely to be the same for these different datasets and that the results from the radio occultation measurements are especially sensitive to height between 45° and 65° latitude.) Considering the different mixes of observation times, heights, and longitudes used to construct Fig. 12, the agreement is probably as good as can be expected for a varying atmospheric circulation. While this comparison does not serve as a stringent check on any of these measurements, it removes any doubt that we are measuring actual windspeeds. Moreover, this comparison also limits the magnitude of any supposed tidal bias in the zonal wind at low latitudes to less than ±5 m s^{-1}.

5. Results

a. Measuring aspects of the circulation

1) DEFINITIONS

The measured wind components as a function of longitude, latitude, and time, $u(\lambda, \theta, t)$ and $v(\lambda, \theta, t)$, can be represented as the sum of a time-averaged flow and a transient eddy flow. The time-averaged flow can be further divided into a zonally symmetric part and a standing wave part, as for the zonal wind:

$$u(\lambda, \theta, t) = \{[u]\} + \{u'\} + u^* \qquad (6)$$

where $\{\ \}$ indicates time averaging, $(\ )^*$ is the deviation from the time average, $[\ ]$ indicates zonal averaging, and $(\ )'$ is the deviation from the zonal average. The standing wave zonal windspeed (longitudinal variations in the time mean zonal flow) is given by

$$\{u'\} = \{u(\lambda, \theta, t) - [u(\lambda, \theta, t)]\}$$
$$= \{u(\lambda, \theta, t)\} - [\{u(\lambda, \theta, t)\}]. \quad (7)$$

If we write

$$\{u\} = U = [U] + U' \quad (8)$$

then

$$\{u'\} = U - [U] = U' \quad (9)$$

and

$$u(\lambda, \theta, t) = [U] + U' + U^* \quad (10)$$

where the transient wave zonal windspeed is given by

$$U^* = u - U. \quad (11)$$

An identical formulation holds for $v(\lambda, \theta, t)$. Note that $[U']$ and $[V'] = 0$, and $\{U^*\}$ and $\{V^*\} = 0$.

2) MEASURING MEAN WINDS

Obtaining zonal averages from the limited longitudinal coverage of *Pioneer Venus* requires that the measurements be averaged over at least 30 days; thus, we define U and V by averages over each imaging period of about 60 days. The reversal of the time and zonal averaging operations in the above expressions is only valid on larger time scales. Since the OCPP data cover several 60–80-day time periods over seven years, the sampling of even larger time scales is also incomplete. These factors limit the time and space resolution of the circulation statistics.

3) MEASURING WIND VARIATIONS

Fourier analysis of the image brightness variations shows that the largest variations occur at the lowest (<5) wavenumbers (Del Genio and Rossow 1982). Analysis of time series of image brightnesses and longitudinally averaged windspeeds reveals two periodic variations with periods near 4 and 5 days (DR90). We isolate these wave modes by compositing our windspeed measurements in 4-day and 5-day rotating reference frames. Although *mean* windspeeds are more uncertain poleward of 40° latitude, time series analysis of the wind *fluctuations* there reveals a statistically significant periodicity in some epochs (DR90), giving us confidence that some eddy information is retrievable at higher latitudes. Solar tidal modes can be isolated by compositing the windspeed measurements in a reference frame that rotates with the sun. Smaller scale (higher wavenumber) wave modes are not detectable with our sparse sampling; variations of the flow on shorter (<60 days) time scales are also not detectable.

4) MEASURING MOMENTUM TRANSPORTS

Measuring correlations of the wind component variations to diagnose momentum transports is also limited by the space–time coverage of the observations to a determination of the time-averaged momentum transport, that is composed of contributions from the mean flow, the standing waves, and the transient waves:

$$\{[uv]\} = [U][V] + [U'V'] + [\{U^*V^*\}]. \quad (12)$$

When the total transport is divided into the time average transports of the mean circulation and the eddy motions, an additional term appears that represents the transport associated with correlated time variations of the mean flow:

$$\{[u][v]\} = [U][V] + \{[U^*][V^*]\}, \text{ and} \quad (13)$$

$$\{[u'v']\} = [U'V'] + [\{U^*V^*\}] - \{[U^*][V^*]\}. \quad (14)$$

If we attempt to infer the values of the mean and eddy momentum transports, averaged over one imaging period, we must assume that the last term in both expressions above is zero, since we must accumulate observations over time to obtain complete longitudinal samples of both the mean and eddy motions. If, however, we calculate the average transport over our whole dataset, then the last term can be evaluated directly from the differences in the mean flow among the five imaging periods.

Since we measure only horizontal winds at one level, we obtain no direct information about vertical momentum transports by the same motions. This prevents us from diagnosing the cloud top momentum balance. The horizontal momentum transport by the mean circulation at one level, for example, may look as though a large unbalanced flux is present, even when the net transport is zero, because the unobserved vertical transports act as "sources/sinks" at that level and the cancelling transport occurs in the "return flow" at another level. Likewise, the relative magnitudes of $[U'][V']$, $[U^*][V^*]$, and $[U][V]$ provide no constraints on the importance of possible superrotation mechanisms. Indirect estimates of vertical eddy transports by specific wave modes are possible if the eddy amplitude is known (DR90).

5) LOCATION OF WINDS

The measurement of cloud feature motions limits our data to a single height interval in the atmosphere. Constraints on the altitude of this level are set by observed variations of the UV contrasts (Kawabata et al. 1980), together with the microphysical and chemical nature of the clouds. Since sulfuric acid, the main cloud constituent, does not absorb at 365 nm, some other substance, such as sulfur (Esposito 1980; Toon et al. 1982; Esposito et al. 1983; see other suggestions by Sill 1983 and Hartley et al. 1989), is required to produce the features. The total optical depth of the cloud is about 30, but cloud mass is spread over more than 20

km of altitude (Knollenberg et al. 1980; Esposito et al. 1983). The haze-like microphysics (Rossow 1978) implies that the absorbing material is also likely to be distributed over considerable altitude.

All of the absorber cannot be below too much nonabsorbing material, otherwise the cloud feature contrast could not be as large as 40% as observed at the larger scales (Travis et al. 1979a). This implies that some absorber must occur at levels where the overlying cloud optical depth is no more than about four, which is equivalent to altitudes > 65 km, based on measurements of the vertical distribution of cloud material (Knollenberg et al. 1980). Measurements of the solar flux deposition also indicate that significant amounts of absorber must lie above about 65 km (Tomasko et al. 1980). On the other hand, the decrease of UV feature contrast at high solar phase angles requires the absorber to be below the main sulfuric acid cloud tops (Travis et al. 1979a), defined by a total optical depth of one and located at approximately 70 km (Kawabata et al. 1980). Thus, we estimate the location of our wind measurements to be at about 67 ± 2 km.

In part C, we show evidence for both semidiurnal and diurnal solar tidal components in the wind variations. Theoretical estimates of the vertical wavelengths of these two tidal modes are 30 and 7 km, respectively (Pechmann and Ingersoll 1984); thus, detection of the diurnal mode suggests that the UV features must represent motions in a layer that is smaller than 7 km. A similar constraint arises from consideration of the implied vertical wavelengths of the transient wave modes (DR90).

The entry probe and cyclostrophic thermal wind profiles, discussed earlier, suggest that vertical zonal wind shears in the vicinity of our measurements are no more than 1–2 m s^{-1}/km. Thus, the uncertainty implied in assigning the OCPP measurements to a particular altitude is equivalent to a windspeed uncertainty of no more than ±5 m s^{-1}.

Limaye (1985) has suggested that latitudinal and/or time variations in the cloud-tracked zonal windspeeds can be explained by a variation of the cloud feature altitudes of least 5–10 km. There is no evidence for such a large variation of cloud height with latitude (Hansen and Hovenier 1974; Kawabata et al. 1980; Lane and Opstbaum 1983; Schofield and Taylor 1983). Our detection of the short vertical wavelength diurnal solar tide over a wide latitude range (see next part) also argues against large vertical variations in the observed level with latitude; however, the time variations of this tidal mode could be caused by small (≈2–3 km) altitude shifts over long time periods. Schofield and Taylor (1983) report a wavenumber 1, longitudinal variation of cloud height of 2 km, apparently associated with the diurnal tide (see part C); this variation could exaggerate the amplitude of the diurnal tide by 2–4 m s^{-1}.

The small persistent asymmetry of wind speeds between hemispheres may indicate a difference in the level viewed by OCPP produced by the predominance of measurements obtained from a Southern Hemisphere vantage point; however, the average distribution of windspeeds obtained from measurements with a vantage point within 5° of the equator exhibits the same hemispheric asymmetry. We, therefore, interpret the changes in windspeed with latitude and longitude, and among the imaging epochs, to represent real variations of the mean circulation and the hemispheric asymmetry as a residual from a sparse sample of a varying circulation.

b. Mean winds and long-term variations

Figure 13 shows the zonal mean wind components averaged over all the *Pioneer Venus* imaging periods; Tables 5 and 6 give the mean values for each imaging epoch. Figure 14 shows the deviations of the zonal mean windspeeds in each imaging period from the average values in Fig. 13. The 3–5 m s^{-1} amplitude of

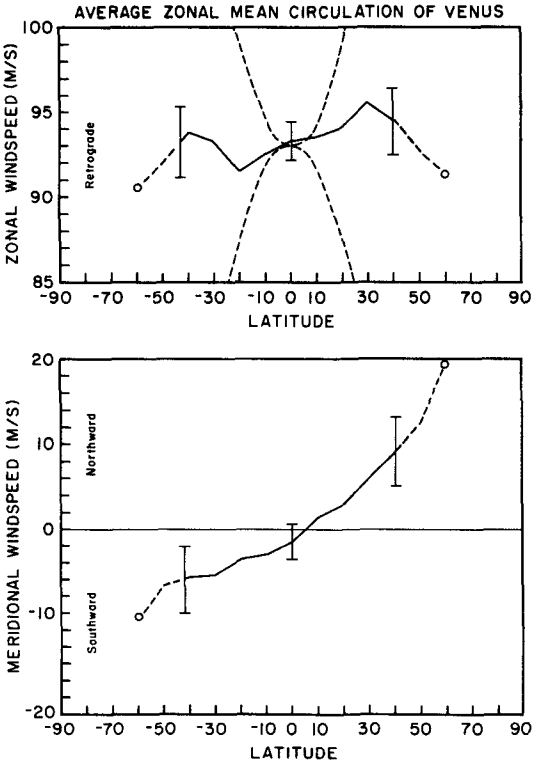

FIG. 13. Zonal mean windspeed components averaged over all imaging periods as a function of latitude: (a) zonal windspeed and (b) meridional windspeed. The dashed curves in (a) represent the windspeeds that would exist at higher latitudes if the equatorial angular momentum were carried poleward conservatively (upper) and if the whole atmosphere rotated like a solid body (lower). Open circles and dashed lines indicate less reliable values based on fewer vectors. Vertical bars indicate estimated uncertainties.

TABLE 5. Mean zonal windspeeds as a function of latitude for each epoch from the average of all vectors with no correction for solar tides. All zonal windspeeds are retrograde. Parentheses indicate larger uncertainties; no value is reported if the number of vectors is less than 10.

Latitude	1979	1980	1982	1983	1985	ALL
−66	—	—	(93.0)	—	—	(93.0)
−62	—	(85.0)	(88.7)	(89.6)	(89.0)	(88.1)
−58	—	(89.1)	(91.4)	(87.3)	(90.6)	(89.6)
−54	—	(89.6)	(90.7)	(93.1)	(89.2)	(90.6)
−50	—	(91.5)	(91.0)	(92.0)	(89.7)	(91.0)
−46	(94.6)	(93.0)	(92.6)	(92.5)	(92.1)	(93.0)
−42	(89.7)	93.8	92.8	95.5	98.1	94.0
−38	93.0	94.8	92.3	93.2	98.8	94.4
−34	95.4	93.5	90.6	92.9	96.0	93.7
−30	95.0	94.3	89.7	93.0	92.1	92.8
−26	94.6	93.0	88.4	90.2	93.6	92.0
−22	93.5	92.2	87.6	90.5	93.3	91.4
−18	94.2	93.3	87.6	90.9	95.0	92.2
−14	93.8	93.2	86.8	90.2	95.6	91.9
−10	95.6	93.0	87.9	89.6	96.3	92.5
−6	94.9	93.2	88.2	89.3	95.4	92.2
−2	94.8	93.7	88.3	89.5	97.1	92.7
2	96.0	94.3	89.1	89.7	96.9	93.2
6	95.1	94.7	90.0	90.3	96.1	93.2
10	95.6	94.2	90.8	90.3	96.0	93.4
14	97.6	94.3	91.6	91.9	98.6	94.8
18	97.3	94.9	91.9	91.5	96.4	94.4
22	96.5	94.2	92.5	91.8	98.7	94.7
26	95.2	96.6	93.0	92.3	99.8	95.4
30	92.0	97.8	95.4	95.2	98.4	95.8
34	91.7	97.7	96.4	94.9	98.7	95.9
38	87.7	96.6	95.6	94.7	97.6	94.4
42	(91.9)	(95.4)	(92.5)	(94.6)	(94.6)	(93.8)
46	(84.8)	(93.2)	(92.7)	(94.4)	(97.8)	(92.6)
50	—	(92.0)	(90.6)	(92.5)	(90.7)	(91.4)
54	—	(91.8)	(88.4)	(95.6)	(93.0)	(92.2)
58	—	(89.0)	(93.1)	(91.7)	(98.8)	(93.2)
62	—	(85.1)	—	(89.9)	(93.2)	(89.4)
66	—	—	—	(97.8)	—	(97.8)

the variations relative to the long-term mean, shown in Fig. 14, is significant, as shown by the error bars (which are twice the formal error estimate); the amplitude of changes from epoch to epoch is slightly larger (Fig. 15). The time scale for these variations is about 1–6 years. The lower limit on the time scale is suggested by changes apparent from 1979–1980; however, the zonal windspeeds in 1982 and 1983 resemble each other closely. The upper limit is set by the resemblance of the zonal windspeeds in 1979 and 1985. However, the fact that no two periods are strictly the same means that the five brief samples we have do not provide a very accurate picture of the average circulation.

The mean zonal flow is approximately symmetrical about the equator and exhibits weak midlatitude jets. Although commonly referred to as the "4-day wind," the rotation period of the cloud top atmosphere on Venus, implied by the zonal flow, makes it more nearly a "5-day wind": the equatorial zonal windspeeds imply rotation periods ranging from 4.6 days in 1985 to 5.0 days in 1982. The mean meridional circulation is also approximately symmetrical about the equator and poleward in both hemispheres. Taken together with the probe wind measurements at lower altitudes and the cyclostrophic zonal winds inferred at higher altitudes, these results are consistent with the presence of a thermally direct Hadley circulation, that is driven by deposition of solar radiation in the upper cloud and/or planetary thermal radiation near cloud base and that extends to at least 60°–70° latitude. The mean zonal flow exhibits the same superrotation as at other altitudes with weak midlatitude jets near the location of peak meridional windspeed.

From a comparison of the zonal flows inferred from *Mariner 10* and the first year of *Pioneer Venus* measurements, Rossow et al. (1980) suggested that the midlatitude portion of this mean circulation vacillated between a jet-like structure and one resembling solid body rotation of the whole cloud top atmosphere. Since the *Mariner 10* results were based on only a 3-day dataset, the magnitude of the jet windspeeds may have been exaggerated (note the reduction of peak wind-

TABLE 6. Mean meridional windspeed as a function of latitude for each epoch from the average of all vectors with no correction for solar tides. Positive meridional windspeeds are northward. Parentheses indicate larger uncertainties; no value is reported if the number of vectors is less than 10.

Latitude	1979	1980	1982	1983	1985	ALL
−66	—	—	(−42.8)	—	—	(−42.8)
−62	—	(−12.8)	(−10.9)	(−21.6)	(−33.4)	(−19.7)
−58	—	(−4.2)	(−6.0)	(−10.7)	(−3.4)	(−6.1)
−54	—	(−5.1)	(−7.0)	(−6.7)	(−6.6)	(−6.4)
−50	—	(−4.4)	(−6.5)	(−8.8)	(−6.7)	(−6.6)
−46	(−5.4)	(−4.9)	(−6.9)	(−8.5)	(−9.5)	(−7.0)
−42	(−16.5)	−5.1	−6.8	−8.9	−5.0	−8.5
−38	−7.5	−5.0	−6.6	−6.5	−2.1	−5.5
−34	−7.9	−4.7	−5.6	−5.9	−6.5	−6.1
−30	−9.3	−4.4	−6.2	−6.7	−5.4	−6.4
−26	−4.7	−2.9	−4.8	−5.3	−8.1	−5.2
−22	−4.4	−2.8	−3.4	−4.0	−9.7	−4.9
−18	−3.1	−1.5	−3.0	−4.0	−13.9	−5.1
−14	−3.5	−0.7	−1.8	−4.2	−11.7	−4.4
−10	−2.4	+0.2	−0.8	−1.2	−12.6	−3.4
−6	−1.1	+1.9	+0.3	−0.8	−9.5	−1.8
−2	−0.3	+3.1	+0.8	−1.0	−11.9	−1.7
2	+1.4	+3.6	+2.2	+1.6	−6.1	+0.5
6	+3.0	+4.0	+3.2	+3.0	−4.4	+1.8
10	+4.7	+4.3	+4.2	+3.7	−0.4	+3.3
14	+5.4	+4.3	+4.1	+4.4	+0.2	+3.7
18	+7.4	+4.6	+5.0	+4.0	+2.5	+4.7
22	+8.2	+5.5	+5.7	+4.3	+3.0	+5.3
26	+10.1	+7.1	+5.5	+5.3	+4.1	+6.4
30	+3.9	+7.9	+8.7	+6.6	+5.6	+6.5
34	+9.2	+9.3	+9.4	+9.3	+8.0	+9.0
38	+12.9	+9.2	+8.0	+12.4	+8.6	+10.2
42	(+20.5)	(+9.6)	(+9.0)	(+12.4)	(+4.9)	(+11.3)
46	(+26.7)	(+9.9)	(+10.0)	(+14.3)	(+1.6)	(+12.5)
50	—	(+10.4)	(+11.8)	(+17.1)	(−3.2)	(+9.0)
54	—	(+13.0)	(+13.9)	(+10.0)	(−17.4)	(+4.9)
58	—	(+17.3)	(+28.0)	(+15.1)	(+16.8)	(+19.3)
62	—	(+38.9)	—	(+29.8)	(+18.5)	(+29.1)
66	—	—	—	(+46.1)	—	(+46.1)

speeds between the results based on a small subset of the data, reported in Suomi 1975, and that in Limaye and Suomi 1981). Averages of our mean zonal windspeeds over 5–10 day periods also show differences as large as 10–20 m s^{-1}. As discussed in section 4, the lower zonal windspeeds at higher latitudes reported for the 1979 imaging period in the earlier OCPP results (Rossow et al. 1980) were exaggerated by the larger proportion of the spurious slow wind vectors in those results. Figure 15 still shows significant variations of the northern midlatitude jet speed, but much less than suggested by the earlier analysis. The overall impression is that variations of the zonal flow at both the equator and midlatitudes contribute to creating a contrast in the zonal flow between them.

The mean zonal flow is compared in Fig. 13 to that expected for poleward transport of the equatorial flow by the Hadley circulation in the absence of any mixing (inversely proportional to cosine of the latitude) and to that expected for very strong horizontal mixing (proportional to cosine of the latitude). The intermediate latitudinal distribution of the actual zonal windspeeds requires the presence of some stirring process, but suggests that the stirring is relatively weak (see section 6).

The actual sequence of events, illustrated in Figs. 14 and 15, suggests more complex variation scenarios. In 1979, the zonal winds at low latitudes were somewhat faster than average, decreasing the contrast with the midlatitude jets (i.e., zonal wind maxima). The Northern Hemisphere jet was weaker than the southern jet. By 1980, the zonal winds at the equator had decreased by about 2 m s^{-1}, while the northern jet strengthened. The decline of the zonal winds at the equator continued into 1982, changing by another 4–5 m s^{-1}. In 1983, the southern jet increased by about 2–3 m s^{-1} with little change elsewhere. In 1985, the equatorial zonal winds increased by 5–6 m s^{-1}, while the jets increased by 1–3 m s^{-1}, returning to a configuration similar to 1979 at the equator and southern midlatitudes but not at northern midlatitudes. Changes in the Hadley circulation between epochs are also suggested in Fig. 15, but they are not always hemispherically symmetric and follow no obvious pattern.

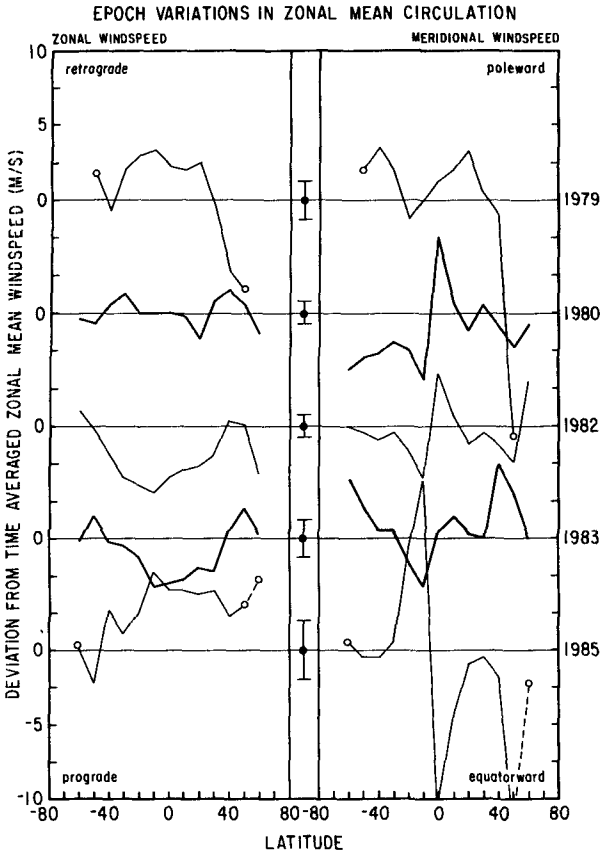

FIG. 14. Deviations of the zonal mean windspeed components from the time-averaged zonal mean values (in Fig. 13) for each imaging epoch as a function of latitude. Positive deviations of zonal windspeed indicate larger retrograde velocities. Positive deviations of meridional windspeeds indicate larger poleward velocities, except at the equator, where positive deviations indicate larger northward velocities. Error bars show twice the formal error based on the number of vectors and the estimated precision of each measurement. Open circles and dashed lines indicate less reliable values based on fewer vectors.

The apparent independence of the changes of the equatorial and midlatitude flows in the two hemispheres may be caused by the small number of samples scattered over many years. The variety of changes between imaging epochs also suggests that we have not seen all possible combinations of strong/weak jets, equatorial flows, and Hadley circulations. This reinforces the caution that the average circulation and its characteristic time variations can be seen only crudely in these results.

c. *Solar tides*

Figure 16 shows the deviations of the 1980 zonal and meridional windspeeds from their zonal mean values when the data are composited in solar fixed coordinates. Both parts of Fig. 16 show clear evidence for significant tidal deviations: the zonal windspeed perturbation amplitude is about 10 m s^{-1} and peaks at the equator near the evening terminator, while the meridional windspeed perturbation amplitude is 4–6 m s^{-1} and peaks at 20°–40° latitude in both hemispheres near local noon. Figure 17 shows that tidal amplitudes are larger than the estimated uncertainties in all epochs. Limaye (1988) also found evidence for solar tides in 1982. The zonal and meridional perturbations are approximately in quadrature, implying significant divergence near the equator near local noon.

Zonal windspeed deviations at the equator exhibit both wavenumber one (diurnal) and two (semidiurnal) variations. Figure 17 compares the windspeed deviations in 1982 to deviations calculated for the sum of two sine functions, one with wavenumber 1 (diurnal) and twice the amplitude of another with wavenumber 2 (semidiurnal) and a small phase difference. Figure 17 also shows the variations of the tides with time, which can be interpreted in terms of a roughly constant semidiurnal component and a variable diurnal component: the diurnal tide amplitude appears to increase from 1979 through 1982, decrease sharply in 1983,

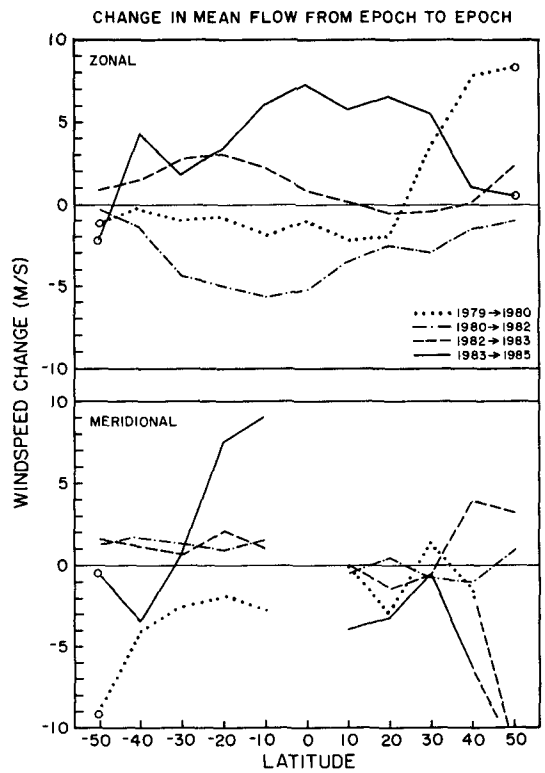

FIG. 15. Latitude distribution of changes in the mean zonal wind components from one imaging period to the next. Positive changes in the zonal windspeed indicate stronger retrograde winds; positive changes in the meridional windspeed indicate stronger poleward flow in each hemisphere. The formal error in the differences varies from less than 1 m s^{-1} at the equator to about 1–2 m s^{-1} at the highest latitudes. Open circles and dashed lines indicate values with much larger uncertainties associated with too few vectors.

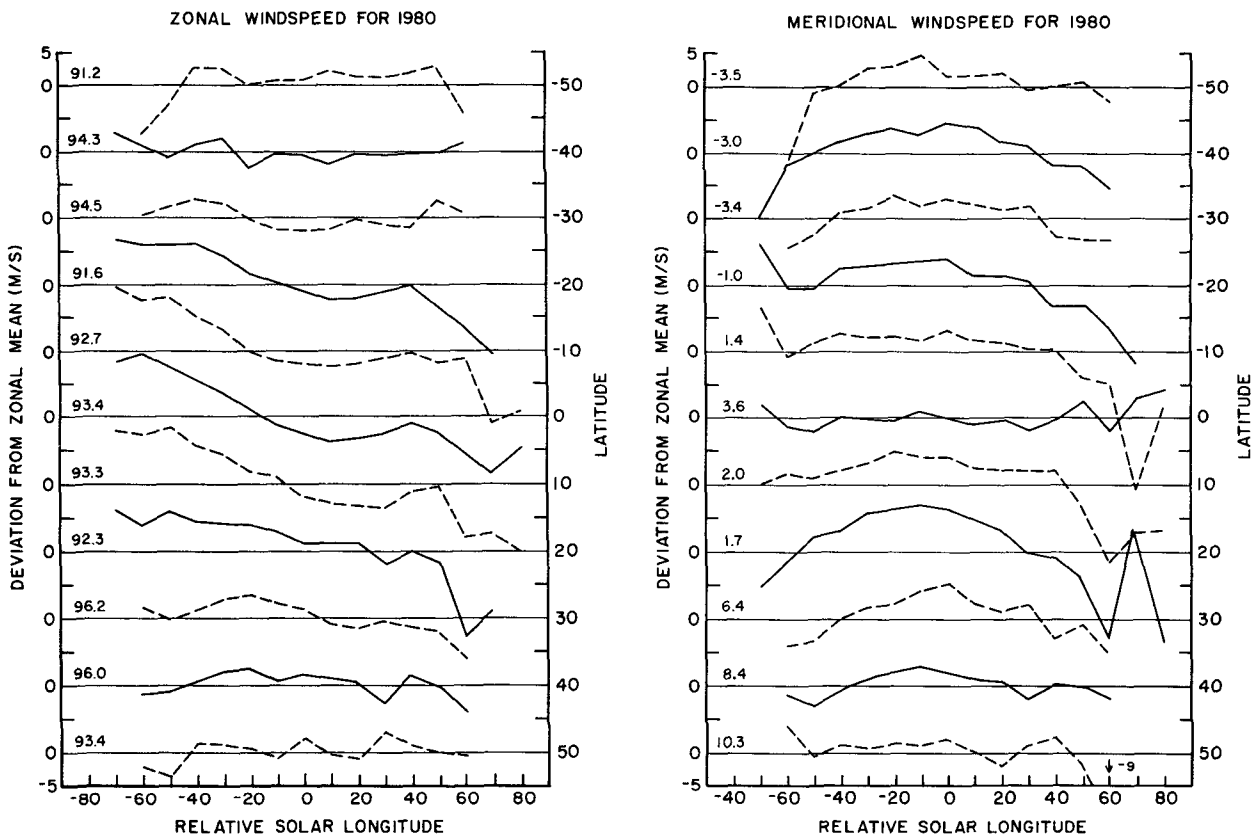

FIG. 16. Deviations of (a) zonal and (b) meridional windspeed components from their zonal means as a function of latitude and relative longitude in solar-fixed coordinates for the 1980 imaging epoch. Positive values represent larger retrograde zonal winds and larger poleward meridional winds, except at the equator where positive deviations represent larger northward winds. The zonal mean windspeed is indicated on the left in each panel.

and begin to grow again in 1985 (Table 7). The meridional deviations seem to be predominantly wavenumber one (though the limited longitude coverage makes this difficult to judge) and to be stronger when the zonal deviations are dominated by the diurnal component. The peak amplitudes of the diurnal and semidiurnal tides appear to be about 10 m s^{-1} and 5 m s^{-1}, respectively. The phases of the two tidal modes seem to be about 20°–40° different; the diurnal mode appears to have peak windspeed near the evening terminator, while the semidiurnal mode has one peak about 30° into the morning quadrant.

The *Pioneer Venus* Orbiter Infrared Radiometer (OIR) detected both diurnal and semidiurnal variations in temperature (Taylor et al. 1980; Schofield and Taylor 1983). Both modes had similar amplitude in the upper clouds, but the semidiurnal mode was predominant above the clouds. The amplitudes (of temperature deviations) also decreased slowly with increasing latitude (Schofield and Taylor 1983; Fels et al. 1984). Our wind perturbations (Fig. 17) show similar behavior in 1979. Simulations by Pechmann and Ingersoll (1984) show that the vertical resolution of the OIR may cause some underestimate of the amplitude of the diurnal mode; a similar effect may occur to a lesser extent in our results.

Although we cannot uniquely relate the temperature phase and the wind phase, because we do not know the precise relative altitudes of our results and those of the OIR, we note that the peak wind divergence for the diurnal mode appears to occur somewhat after noon (the peak meridional wind perturbation occurs after noon when the diurnal mode is largest in Fig. 17), whereas the peak convergence of the semidiurnal mode appears to occur before noon. The OIR measurements also imply peak diurnal temperature deviations in the afternoon and peak semidiurnal deviations in the morning (Schofield and Taylor 1983; Pechmann and Ingersoll 1984).

Given the small vertical wavelength estimated for the diurnal mode (7 km), the large variability of its amplitude could be caused either by a small shift in the altitude of the observed layer or by an actual change in the diurnal mode amplitude. The change in equatorial mean zonal windspeed from 1979 to 1982, for example, implies a change in the vertical wavelength

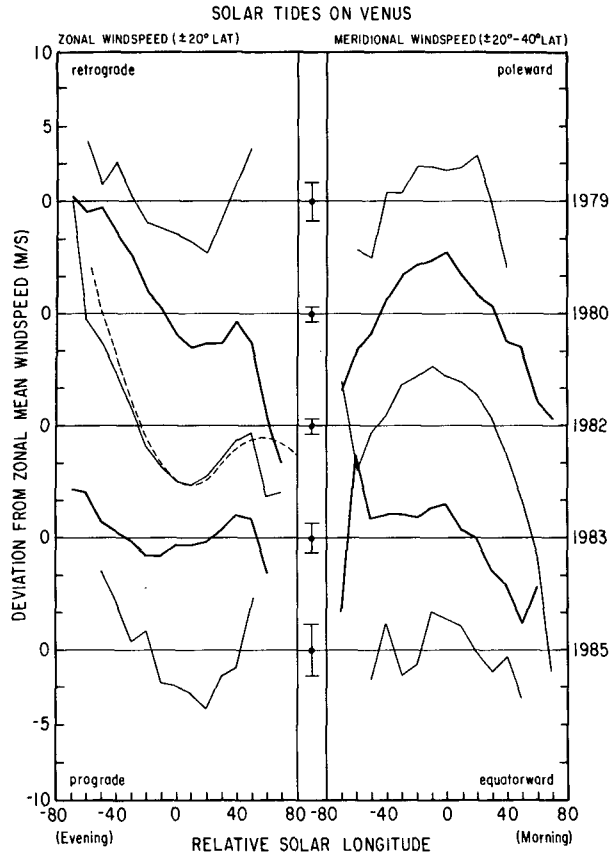

FIG. 17. Deviations of the windspeed components from their zonal means as a function of relative longitude in solar-fixed coordinates for each imaging epoch. The subsolar point is at zero longitude with the evening quadrant to the left and morning quadrant to the right. Zonal windspeed deviations are shown for the equatorial zone, with positive values representing larger retrograde velocities, and meridional windspeed deviations are shown for midlatitudes, with positive values representing larger poleward velocities. Midlatitude values are an average of both hemispheres. Error bars are twice the formal error estimate. The dashed curve in the 1982 zonal windspeed panel illustrates the windspeed obtained from the sum of two sine functions, one with wavenumber 1 and twice the amplitude of another with wavenumber 2 and a 22.5° phase difference.

of as much as 1 km (based on scaling from Fels et al. 1984), which could cause an apparent amplitude change as well.

Since our observations cover a limited range of relative solar longitudes, the tides can bias the the inferred zonal mean windspeeds. As Fig. 17 shows, the tidal zonal wind amplitudes are small compared to the mean zonal flow and the phase makes the wind deviations roughly antisymmetric about the subsolar point. Using the illustrative fit for the 1982 data, we estimate that the bias in the zonal mean windspeeds is no more than 2 m s^{-1} (the sign is difficult to determine) when the diurnal component is large and somewhat less when the semidiurnal component predominates. The same is not necessarily true for the meridional wind, whose tidal component tends to peak near the subsolar longitude (Fig. 17); thus, the cloud-tracked mean meridional winds may be overestimated. In fact, our 1982 mean meridional wind is about half as strong as that of Limaye (1988), while our tidal meridional wind is about twice as strong. This difference is associated with a larger range of solar longitudes covered in our analysis than in Limaye's. Comparison of the windspeeds measured by the *Pioneer Venus* Day and Night probes at 62 km suggests, however, that the tidal biases cannot be too large for either wind component (Counselman et al. 1980).

d. Transient waves

Time series analysis of daily, longitudinal averages of image brightness and zonal and meridional windspeeds indicates the presence of two statistically significant periods, one (4 days) shorter and one (5 days) longer than the rotation period implied by the mean zonal flow (DR90). We estimate the structure and amplitudes for these two waves by compositing our measurements into longitude systems that rotate with these two periodicities. Figures 18–21 show the resulting latitude–"longitude" distributions of zonal and meridional winds (the absolute longitudes are arbi-

TABLE 7. Latitudinal distributions of windspeed standard deviations and various estimates of wave amplitudes. Values in parentheses are for the meridional component.

Latitude zone	Total std. dev.	Time series variance	4-day wave	5-day wave	Solar tides
1979					
−40° to −20°	15 (15)	—	5 (5)	5 (6)	1 (6)
−10° to 10°	12 (13)	—	5 (4)	6 (3)	5 (2)
20° to 40°	15 (16)	—	4 (5)	5 (7)	1 (4)
1980					
−40° to −20°	14 (15)	6	2 (1)	1 (1)	3 (7)
−10° to 10°	12 (15)	7	3 (2)	2 (2)	10 (3)
20° to 40°	15 (16)	6	2 (1)	2 (2)	3 (7)
1982					
−40° to −20°	12 (15)	6	—	—	5 (5)
−10° to 10°	10 (13)	6	2 (1)	1 (1)	18 (2)
20° to 40°	13 (16)	5	—	—	3 (7)
1983					
−40° to −20°	14 (15)	—	4 (2)	4 (4)	1 (5)
−10° to 10°	12 (15)	—	5 (3)	5 (3)	3 (2)
20° to 40°	15 (17)	—	4 (2)	3 (4)	3 (4)
1985					
−40° to −20°	13 (22)	—	4 (6)	5 (7)	6 (6)
−10° to 10°	11 (20)	—	5 (8)	9 (10)	7 (4)
20° to 40°	14 (18)	—	4 (6)	6 (8)	4 (4)

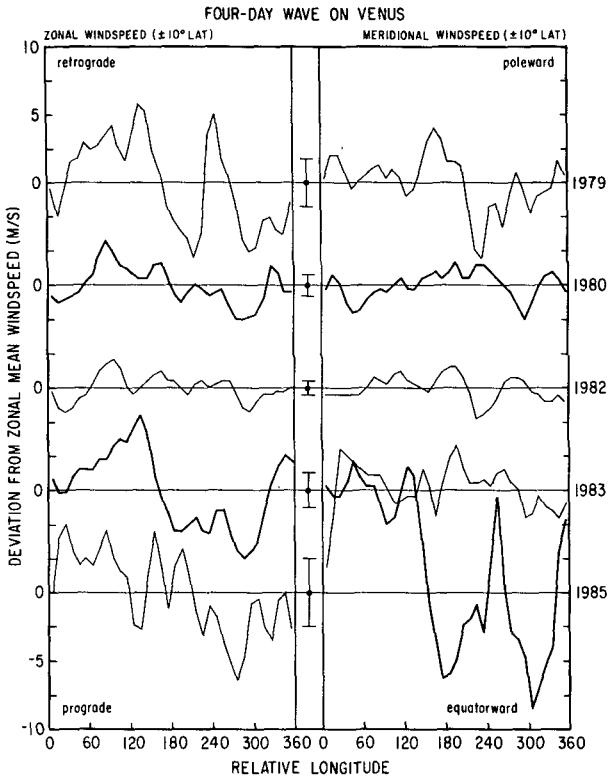

FIG. 18. Deviations of the zonal and meridional windspeeds at the equator from their respective zonal means as a function of relative longitude in a coordinate frame rotating with a 4-day period for each imaging period. See caption to Fig. 14 for other details.

trary). The estimated wave amplitudes (Table 7) are lower limits because, unless the actual wave periods are exactly 4 and 5 days, some "smearing" is unavoidable. Nevertheless, the inferred wave amplitudes are larger than the estimated uncertainties except in 1982 for the 4-day wave and in both 1980 and 1982 for the 5-day wave.

The evolution of the 4-day wave from one imaging period to the next (Figs. 18 and 19) is consistent with the analysis of image brightness variations (DR90) in showing a decreasing amplitude from 1979 through 1982 and an increasing amplitude from 1982 to 1985. (The wavenumber and character of the very small variations in 1982 suggests that a weak 4-day wave may still be present). The amplitude of the zonal component appears to be weaker at higher latitudes than lower, while the behavior of the meridional component is more varied. Figure 19 shows that the midlatitude variations are approximately symmetric about the equator in both amplitude and phase. These features reinforce our identification of the 4-day variations as the gravest mode Kelvin wave (DR90).

We have assumed in this treatment of the data and in the analysis in DR90 that the 4-day variability is predominantly wavenumber 1. Figures 18 and 19 support this supposition, but the presence of secondary maxima and minima also suggests that a separate wavenumber 2 may also be present, especially in 1985, and that it may not be hemispherically symmetric.

Figures 20 and 21 show the windspeed deviations associated with the 5-day wind and brightness variation period. The zonal wind variations are larger near the equator than at midlatitudes, while the meridional variations are larger at midlatitudes. This behavior is consistent with our identification of this mode as a Rossby–Haurwitz wave (DR90). The 5-day wave mode amplitude starts out somewhat smaller than the 4-day wave mode in 1979 and decreases more quickly, disappearing entirely in 1982. The 5-day wave reappears in 1983, again at lower amplitude than the 4-day wave, and grows somewhat by 1985.

Higher wavenumbers at the 5-day period, especially in 1983, seem hemispherically asymmetric. Rossow and Williams (1979) showed that both symmetric and asymmetric planetary modes can occur. The impression that the higher wavenumber mode is more variable is consistent with the fact that all higher wavenumber modes are barotropically unstable (Rossow and Williams 1979).

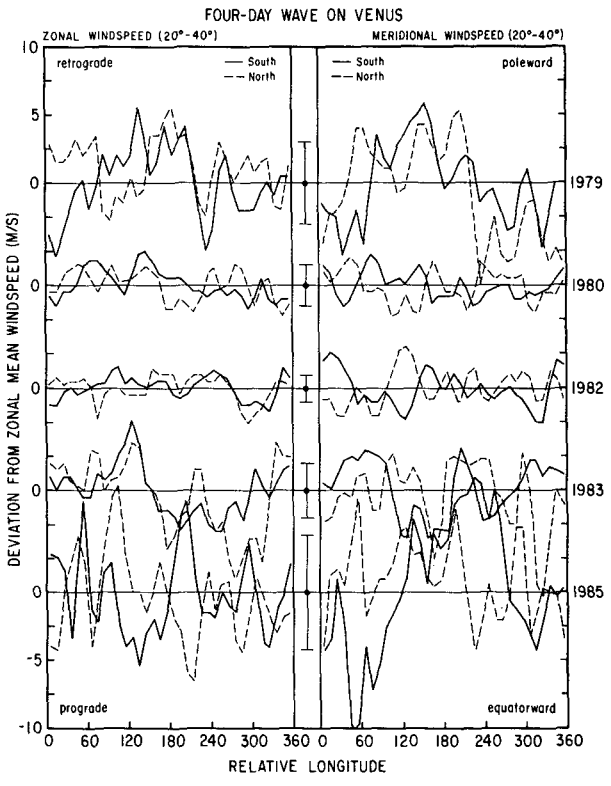

FIG. 19. Deviations of the zonal and meridional windspeeds at midlatitudes from their respective zonal means as a function of relative longitude in a coordinate frame rotating with a 4-day period for each imaging period. The solid lines show the values for the southern hemisphere and the dashed lines show them for the northern hemisphere. See caption to Fig. 14 for other details.

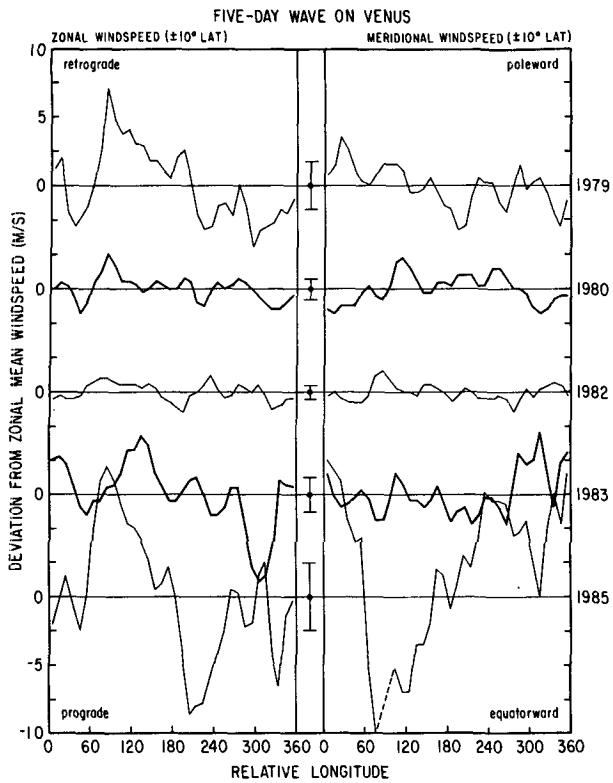

FIG. 20. As in Fig. 18 but for a coordinate frame rotating with a 5-day period.

The longitudinal deviations of the winds from their mean values is strong evidence for the presence of wavenumber 1 waves. The correlations of observed variations of windspeeds and image brightness (DR90) establishes the link between the largest amplitude brightness and wind variations suggested by Del Genio and Rossow (1982). The results, together, show that the largest amplitude wave motions occur at the lowest wavenumbers, consistent with theoretical expectations (Rossow and Williams 1979) and three-dimensional GCM simulations (cf., Rossow 1983; Del Genio and Suozzo 1987).

e. *Standing waves*

We searched for standing waves (phases fixed with respect to the solid planet) by examining deviations of the windspeeds with longitude from their zonal averages. There are three difficulties. (i) The density of wind vectors in a single imaging epoch limits longitude coverage to less than 90°. (ii) Observations at each longitude occur at about the same solar phase in every imaging epoch, making it difficult to separate any standing waves from solar tides. (iii) The longitudes at either end of the range are observed at opposite ends of the imaging period and for less time than longitudes near the center. Consequently, the effects of transient waves cannot be averaged out completely and averaging of the results over all imaging epochs does not reduce these systematic effects. We see no consistent pattern indicating the presence of a standing wave, but the difficulties mentioned above only allow us to constrain the amplitude of such a wave to less than about 5 m s^{-1}.

f. *Momentum transports*

The time-averaged vorticity of the zonal mean circulations increases monotonically from the equator to the highest latitudes we observe, which indicates that the mean zonal flow at this level is stable against shear instability *on average*. This does not preclude the occurrence of shear instability, however, but only indicates that such instability, if it occurs, is sporadic rather than continuous. Such situations occur in slowly rotating GCM simulations (Rossow 1983; Del Genio and Suozzo 1987) and are consistent with weak forcing for the midlatitude jets. Moreover, the location of our observations below and equatorward of the peak of the zonal jet, inferred from the thermal structure, weakens indications of shear instability; the zonal flows calculated by Newman et al. (1984) and Walterschied et al. (1985) imply an extremum of the vorticity at 60°–70° latitude.

Horizontal transports of momentum by the mean and eddy circulations are calculated for each imaging

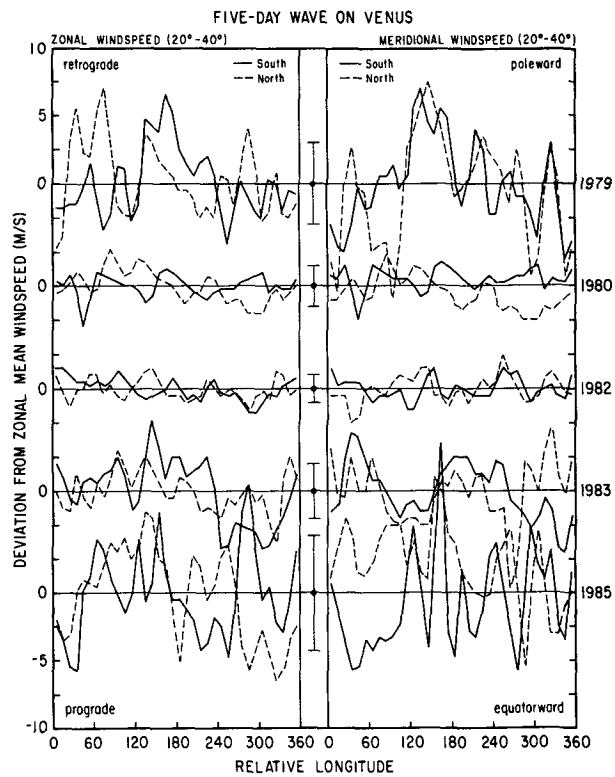

FIG. 21. As in Fig. 19 but for a coordinate frame rotating with a 5-day period.

TABLE 8. Components of the time-averaged momentum transport in $m^2 s^{-2}$; positive values indicate northward transport of retrograde momentum. See (13) and (14) for definitions of the components.

Lat (deg)	$[U][V]$	$\{[U^*][V^*]\}$	$\{[u][v]\}$	$\{[u'v']\}$	$[U'V']$	$\{[U^*V^*]\}$	$-\{[U^*][V^*]\}$
−50	−603.1	−171.5	−774.6	172.8	2.0	−0.7	171.5
−40	−477.1	−67.2	−544.3	58.6	0.9	−9.5	67.2
−30	−474.3	−93.1	−567.4	95.1	−0.2	2.2	93.1
−20	−507.1	81.5	−425.6	−85.9	0.0	−4.4	−81.5
−10	−268.8	63.8	−205.0	−58.1	2.1	3.6	−63.8
0	−5.7	14.1	8.4	−13.3	0.8	0.0	−14.1
10	302.9	−63.2	239.7	77.8	1.0	13.6	63.2
20	414.3	−73.1	341.2	85.1	1.8	10.2	73.1
30	606.0	−16.6	589.4	37.5	0.6	20.3	16.6
40	894.7	90.1	984.8	−59.2	5.3	25.6	−90.1
50	699.9	−59.8	640.1	91.3	−10.2	41.7	59.8

epoch and over the whole dataset, using (13) and (14). Table 8 shows the results for the whole dataset, where we average over each imaging period to eliminate contributions from short-term variations, to accumulate complete longitudinal samples, and to isolate the contributions of long-term variations (see discussion in part A); these results will be called the "long-term" transports. Table 9 shows the mean and eddy transports calculated for each imaging period, where we include only the short-term variations and must assume that the mean flow does not change over the period. These results will be called the "short-term" transports. Horizontal momentum transports are also calculated separately for the solar tides, but their magnitudes are <30% of the total eddy transport with highly variable direction.

The long-term transports by the zonal mean circulation carry retrograde zonal momentum generally poleward in both hemispheres in all epochs; the short-term magnitude varies by about 15%–100% (Table 9). The long-term eddy transports carry retrograde zonal momentum away from the equator at lower latitudes and towards the equator at higher latitudes, suggesting convergence near the zonal jet latitudes. However, the long-term eddy transport is dominated by the correlated changes in the mean zonal flow with time; the explicit terms for the long-term standing and transient eddy transports are small (Table 8). In other words, the largest contribution to long-term eddy transport is the time variations of the mean flow that occur at shorter time scales, variations likely to be associated with shorter-term eddies. With the sparse and incomplete sampling that we have in our data, the short-term eddy transports inferred may be partially cancelled by the changes in the zonal mean flow that these eddies cause.

The strong variations in the short-term eddy momentum transports (≈100%), shown in Table 9, demonstrate their sporadic nature; note especially that in 1985 the short-term transports exhibit a reversal of direction in both hemispheres that may be associated with growing transient waves. However, the removal of the inferred tidal transports changes these results significantly; with our incomplete sample of solar longitudes, we cannot properly account for the solar tide contributions to the total eddy transports.

The predominance of the changing zonal mean flow in the long-term eddy transports, and the large differ-

TABLE 9. Mean and eddy components of the momentum transport in $m^2 s^{-2}$ for each imaging period; positive values indicate northward transport of retrograde momentum. See (13) and (14) for definitions of the components.

Lat	1979		1980		1982		1983		1985	
(deg)	$\{[u][v]\}$	$\{[u'v']\}$	$\{[u][v]\}$	$\{[u'v']\}$	$\{[u][v]\}$	$\{[u'v']\}$	$\{[u][v]\}$	$\{[u'v']\}$	$\{[u][v]\}$	$\{[u'v']\}$
−50	−843.6	−84.7	−434.0	−13.1	−483.9	11.2	−740.8	−3.3	−488.2	−1.5
−40	−776.8	−80.7	−408.2	−30.4	−527.9	−3.6	−661.2	−40.7	−73.1	112.4
−30	−716.1	−7.2	−337.3	−6.6	−400.0	−16.4	−376.0	−0.2	−254.1	74.4
−20	−567.3	1.3	−159.3	−10.3	−246.6	−3.1	−493.5	8.9	−1055.5	−16.4
−10	−164.1	4.5	79.2	−7.9	−38.6	−0.1	−136.7	24.9	−1199.9	49.8
0	114.3	−0.8	122.5	21.4	145.1	5.0	104.6	−16.9	−790.7	−47.1
10	375.2	19.4	276.7	30.4	367.5	12.2	286.7	9.4	193.9	−38.0
20	721.6	22.0	201.5	10.6	362.2	11.3	171.7	16.6	101.7	−49.0
30	660.9	33.3	616.4	25.2	450.5	43.6	563.6	−8.5	600.4	−24.9
40	843.6	4.7	1112.2	28.7	886.6	32.9	1165.1	54.7	601.0	33.8
50	261.8	145.9	771.6	43.3	916.0	24.1	1223.6	124.7	−474.3	53.7

ences between the long-term and short-term patterns, suggest that we mistake time variations of the mean motions for wave motions. We conclude that our data sample is too sparse to diagnose the complete horizontal momentum transports, even at one level.

6. Comments

a. Observational limitations

The wind measurements from OCPP cloud-tracked winds and from the RSS and OIR inferences from the thermal structure constitute the most extensive information about the circulation of Venus, but these data are still very limited in key ways. The RSS and OIR data provide our only information about the vertical and latitudinal distribution of the long-term average temperature and zonal winds above about 50 km, but they do not provide information about meridional or eddy winds. The OCPP data provide the only long-term climatological dataset for the mean and eddy, zonal and meridional winds, but only at one level in lower latitudes. The entry probes provide some descriptive information about winds and temperature below the clouds, but do not cover either latitude or longitude adequately nor give any idea of wave activity (except for a crude estimate of eddy amplitude that comes from differences among probe measurements).

The larger number of vectors obtained with the automated analysis of OCPP images, compared with the manual tracking technique, enabled us to separate these measurements somewhat to isolate several types of wave motions, but only after averaging over rather long time periods in order to observe all wave phases. This averaging may alias inferred eddy momentum transports significantly. Because the measurements are confined to lower latitudes ($\leqslant 40°$) and one altitude, we cannot integrate the measured horizontal momentum transports over the whole circulation to determine net momentum fluxes and the momentum balance. We cannot measure vertical momentum transports at all; continuity constraints on atmospheric motions usually insure that the net flux divergence results from a *difference* between the horizontal and vertical flux divergences. These factors are sufficient to explain the apparent imbalance between mean and eddy momentum transports.

b. Mean circulation near cloud tops

We presently have two incomplete hypotheses for the maintenance of superrotation of the cloud level atmosphere: that angular momentum is supplied by the vertical momentum transport of a "moving flame" process or vertically propagating solar tides (Fels and Lindzen 1974; Fels et al. 1984; Pechmann and Ingersoll 1984; Baker and Leovy 1987) or that the angular momentum is supplied by the combined action of the Hadley circulation and large scale waves (Gierasch 1975; Rossow and Williams 1979). [Hou and Farrell (1987) and Gierasch (1987) propose a spectrum of gravity waves as a source of vertical momentum transport; see Young et al. (1987)]. The first hypothesis is incomplete because the existing studies either ignore the Hadley circulation or impose an initial superrotation, even though the presence of a Hadley circulation, with the observed mean zonal winds, implies significant horizontal and vertical momentum transports (Hou and Goody 1985). In addition, the sink of momentum that balances the tidal supply is not identified, but rather represented by an assumed ad hoc diffusion or Rayleigh friction. The second hypothesis can provide a balanced flow without invoking additional types of motion (e.g., Rossow 1983; Del Genio and Suozzo 1987), but does not adequately consider the effects of complex vertical structure on the vertical momentum transports nor the consequences of transports by other wave modes that are observed to be present.

We have identified the simultaneous presence of at least two solar tidal modes and a wave mode that may be associated with shear instability of the midlatitude zonal jets, together with an additional planetary scale Kelvin wave (DR90). All of these wave types may play some role in the momentum balance of the cloud level atmosphere: they can either be sources or sinks of momentum and may even change roles with altitude.

If the distribution of zonal winds were controlled solely by the momentum conserving advection of the Hadley circulation, we would expect to see much larger shears in both latitude and altitude than we do see (Rossow 1985). Hence, a predominant role of the wave transports is to balance the implied mean flow transport. The sum of horizontal and vertical mixing by eddies must be comparable to the Hadley transport, however, because the zonal wind profile is neither that of conservation of angular momentum (Hadley transport predominant) nor that of solid rotation (horizontal mixing of angular momentum predominant). At the one level we observe and over lower latitudes, the horizontal transport by the mean flow is a local sink of momentum; the horizontal transport by eddies cannot be accurately diagnosed. The strength of vertical momentum mixing is difficult to estimate; but indirect estimates (DR90) suggest that horizontal and vertical eddy mixing could be of similar magnitude. The general weakness of the *net* forcing for cloud level flows is suggested by the long time scales and small amplitudes of the variations, together with the small wave amplitudes.

Changes that occurred in the Hadley flow are irregular and hard to interpret because they exhibit hemispheric asymmetry. The variations may be the consequence of dynamic feedbacks between the mean flow and the wave motions, much as the mean meridional circulation on Earth is determined in part by eddy momentum transports (Rind and Rossow 1984). Such interactions could explain why the cloud-tracked meridional winds are stronger than those expected for a

thermally driven circulation (cf. Hou and Goody 1985; Baker and Leovy 1987), although the effects of our limited diurnal sampling may also be a factor.

We are left with the suggestive positive correlations between the long-term changes in equatorial zonal winds and the amplitudes of the 4-day and 5-day waves and the negative correlation with the amplitude of the diurnal tide (Figs. 14, 17, 18 and 20). Our time sampling is too coarse to determine whether the equatorial zonal flow decreases because of weakening of the action of the 4-day and 5-day waves (see DR90) or because of a strengthening of the action of the diurnal tidal mode. The short vertical wavelength of the diurnal tide and its sensitivity to changes in static stability or zonal wind shear (Fels and Lindzen 1974; Fels et al. 1984) could explain an apparent change in its amplitude because the zonal flow has changed. Either way, we suggest that the 4-day and 5-day waves combine to supply momentum to the equatorial flow and that the tide and Hadley circulation remove it (DR90). Leovy (1973) first suggested a possible role for a Kelvin mode in the momentum balance on Venus.

c. *Waves*

The 4-day Kelvin mode and the 5-day Rossby-Haurwitz mode are the two gravest modes possible on a sphere (Longuet-Higgins 1968). Uniform forcing of an atmosphere with a vertical shear in the zonal flow, like that observed by the probes, produces significant responses for these two wave modes (Covey and Schubert 1982). Two sources of wave energy at planetary scales have been suggested: linear barotropic instability studies suggest a range of wavenumbers from 2–4 and from 7–11 (Travis 1978) and Young et al. (1984) suggest the possibility of baroclinic instability at higher latitudes in the high shear and low static stability layers near cloud base, with the largest linear growth rates at wavenumbers 4–6. The size spectrum of UV features suggests a relative minimum of power near wavenumber 10, which is consistent with a relative maximum near wavenumbers 3–5 (Rossow et al. 1980; Del Genio and Rossow 1982). Thus, the instability of the zonal flows may produce wave modes with wavenumbers ≈ 4; the subsequent barotropic cascade of their energy into wavenumber 1 by nonlinear interactions (cf., Rossow and Williams 1979; Hendon and Hartmann 1985) can explain the predominance of a wavenumber 1, Rossby-Haurwitz mode. DR90 suggest that the Kelvin mode is stimulated by the Rossby-Haurwitz mode; such interactions are often seen in other studies (e.g., Simmons et al. 1983; Young et al. 1984; Hendon and Hartmann 1985).

The coherence of the 5-day motions between the hemispheres, suggested in Fig. 21 (see also DR90), can be explained by this cascade of energy from higher wavenumbers to wavenumber 1 in a weakly forced circulation, even if the instabilities of the midlatitude zonal jets are not coordinated. If the midlatitude jets are fed by advection of the equatorial zonal flow by the Hadley circulation and limited by shear instability, then they would be expected to be approximately symmetric in strength, as they are observed to be, because of the symmetry of thermal forcing for the Hadley circulation. If the instability of the zonal jets creates eddy kinetic energy in a *statistically* symmetric fashion, then most of the cascade of energy would enter the symmetric wavenumber 1 mode. If the forcing is weak, the circulation retains little memory of the location and timing of the forcing. Moreover, in a mean flow containing net angular momentum, the symmetric mode is strongly preferred (Rossow and Williams 1979).

Since the efficiency of forcing of the tides is dependent on the mean zonal windspeed (Fels and Lindzen 1974), which affects the forcing frequency, the fact that the periods of the two transient wave modes are slightly shorter and slightly longer than the forcing period for the tides may be a hint that the interaction of all these waves somehow serves to establish the zonal flow that establishes this relationship of phase speeds.

d. *Status*

A definitive explanation of the superrotation of Venus' atmosphere is still not possible. Only one general circulation model gets strong superrotation (Williams 1988); but this occurs only with an excessively large diurnal tide, which is inconsistent with the observations. Other models do not get very strong superrotations (Rossow 1983; Covey et al. 1986; Del Genio and Suozzo 1987). The result of Williams (reported earlier in Williams and Holloway 1982) can be interpreted to mean that the problem with the other models is that the efficiency of the horizontal wave mixing is not high enough compared to the Hadley circulation transport (Rossow 1985); however, the vertical resolution of these GCM calculations is also too coarse to simulate tides and other short wavelength gravity waves realistically. Alternatively, excessive vertical mixing due to convection (a crudely parameterized process in all GCMs) or ad hoc diffusion may limit the superrotation attained in the GCMs (Rossow 1983; Del Genio and Suozzo 1987).

Diagnosis of the eddy momentum transports required to maintain the observed zonal flow implies strong vertical and horizontal exchanges within the cloud layer but extremely weak vertical fluxes in the deep atmosphere (Hou and Goody 1985).[5] The failure to detect strong horizontal eddy momentum fluxes at one level may be caused by the limited longitude sampling or may be a signal that small (unseen) scale wave

[5] This weak flux is balanced by ad hoc diffusion in the analysis of Hou and Goody; but since this diffusion also alters the vertical transport by the mean flow, it is hard to evaluate the validity of this inference.

modes play more of a role (at least at this level). Since we detect more waves than needed for all of the hypotheses, but cannot measure their complete heat and momentum transports, we cannot identify the key processes maintaining the cloud level circulation.

No new data will be forthcoming in the near future as no spacecraft missions with atmospheric objectives are being planned for Venus[6] and Earth-based observations are strongly limited by solar interference and observing geometry constraints. Moreover, limiting the measurements to those in reflected sunlight and emitted thermal radiation precludes observations of the whole circulation. Microwave measurements have not yet been exploited for atmospheric observations. Further progress could come from long-term, multispectral observations (UV to near-IR, thermal IR to microwave) from orbiting spacecraft and from long-lived balloons and surface stations.

Acknowledgments. Sanjay Limaye developed early versions of our digital tracking method; subsequent improvements were made by Edward Kinsella and Andrew Abrams. Processing of the large dataset was carried out by several undergraduate students at Columbia University: Kamal Abdullah, Richard Campos, Antonia Lioudakis and David Miller. Early analyses of the data were carried out by Kinsella, Abdullah, and Abrams. Graphics were drawn by Lilly Del Valle with help from Jose Mendoza; word processing was done by Mary Garcia and Elizabeth Devine. We thank Conway Leovy and Richard Goody for thoughtful comments and an anonymous reviewer for helpful suggestions. We also thank Gareth Williams for many thought-provoking conversations over the years and Larry Travis (OCPP Principal Investigator) for assistance in data processing and advice on analysis strategy. Support for this work was provided by the NASA *Pioneer Venus* Project.

REFERENCES

Baker, N. L., and C. B. Leovy, 1987: Zonal winds near Venus' cloud top level: A model study of the interaction between the zonal mean circulation and the semidiurnal tide. *Icarus,* **69,** 202–220.

Beebe, R. F., 1972: Ultraviolet clouds on Venus: Observational bias. *Icarus,* **17,** 602–607.

——, A. P. Ingersoll, G. E. Hunt, J. L. Mitchell and J.-P. Muller, 1980: Measurements of wind vectors, eddy momentum transports, and energy conversions in Jupiter's atmosphere from *Voyager 1* images. *Geophys. Res. Lett.,* **7,** 1–4.

Belton, M. J. S., G. R. Smith, G. Schubert and A. D. Del Genio, 1976b: Cloud patterns, waves and convection in the Venus atmosphere. *J. Atmos. Sci.,* **33,** 1394–1417.

——, ——, D. A. Elliot, K. Klaasen and G. E. Danielson, 1976a: Space-time relationships in the UV markings on Venus. *J. Atmos. Sci.,* **33,** 1383–1393.

Betz, A. L., M. A. Johnson, R. A. McLaren and E. C. Sutton, 1976: Heterodyne detection of CO_2 emission lines and wind velocities in the atmosphere of Venus. *Astrophys. J.,* **208,** L141–L144.

Blamont, J. E., R. E. Young, A. Seiff, B. Ragent, R. Sagdeev, V. M. Linkin, V. V. Kerzhanovich, A. P. Ingersoll, D. Crisp, L. S. Elson, R. A. Preston, G. S. Golitsyn and V. N. Ivanov, 1986: Implications of the VEGA balloon results for Venus atmospheric dynamics. *Science,* **231,** 1422–1425.

Boyer, C., 1973: The 4-day rotation of the upper atmosphere of Venus. *Planet. Space Sci.,* **21,** 1559–1561.

——, and H. Camichel, 1961: Observations photographiques de la planete Venus. *Ann. Astrophys.,* **24,** 531–535.

——, and P. Guerin, 1966: Mise en evidence directe, par la photographie, d'une rotation retrograde de Venus en 4 jours. *C. R. Acad. Sci.,* **263,** 253–255.

——, and P. Guerin, 1971: Irregularities in the four day rotation period of the Y-shaped formations in the upper atmosphere of Venus, and their correlation with the surface rotation. *C. R. Acad. Sci. Paris,* **273B,** 154–157.

Burpee, R. W., and R. J. Reed, 1982: Synoptic-scale motions. *The GARP Atlantic Tropical Experiment. (GATE)* Monograph., GARP Publ. Ser. No. 25, World Meteorological Organization, 61–120.

Caldwell, J., 1972: Retrograde rotation of the upper atmosphere of Venus. *Icarus,* **17,** 608–616.

Counselman, C. C., S. A. Gourevitch, R. W. King, G. B. Loriot and E. S. Ginsberg, 1980: Zonal and meridional circulation of the lower atmosphere of Venus determined by ratio interferometry. *J. Geophys. Res.,* **85,** 8026–8030.

Covey, C., and G. Schubert, 1982: Planetary-scale waves in the Venus atmosphere. *J. Atmos. Sci.,* **39,** 2397–2413.

——, E. J. Pitcher and J. P. Brown, 1986: General circulation model simulations of superrotation in slowly rotating atmospheres: Implications for Venus. *Icarus,* **66,** 380–396.

Crisp, D., W. M. Sinton, K-W. Hodapp, B. Ragent, F. Gerbault, J. H. Goebel, R. G. Probst, D. A. Allen, K. Pierce and K. R. Stapelfeldt, 1989: The nature of the near-infrared features on the Venus night side. *Science,* **246,** 506–509.

Del Genio, A. D., and W. B. Rossow, 1982: Temporal variability of ultraviolet cloud features in the Venus stratosphere. *Icarus,* **51,** 391–415.

——, and R. J. Suozzo, 1987: A comparative study of rapidly and slowly rotating dynamical regimes in a terrestrial general circulation model. *J. Atmos. Sci.,* **44,** 973–986.

——, and W. B. Rossow, 1989: Planetary scale waves and the cyclic nature of cloud top dynamics on Venus. *J. Atmos. Sci.,* **47,** 293–318.

Dollfus, A., 1975: Venus: Evolution of the upper atmospheric clouds. *J. Atmos. Sci.,* **32,** 1060–1070.

Esposito, L. W., 1980: Ultraviolet contrasts and the absorbers near the Venus cloud tops. *J. Geophys. Res.,* **85,** 8151–8157.

——, and L. D. Travis, 1982: Polarization studies of the Venus UV contrasts: Cloud height and haze variability. *Icarus,* **51,** 374–390.

——, R. G. Knollenberg, M. Ya. Marov, O. B. Toon and R. P. Turco, 1983: The clouds and hazes of Venus. *Venus,* D. M. Hunten, L. Colin, T. M. Donahue and V. I. Moroz, Eds., University of Arizona, 484–564.

Fels, S. B., and R. S. Lindzen, 1974: The interaction of thermally excited gravity waves with mean flows. *Geophys. Fluid Dyn.,* **6,** 149–191.

——, J. T. Schofield and D. Crisp, 1984: Observations and theory of the solar semidiurnal tide in the mesosphere of Venus. *Nature,* **312,** 431–434.

Fujita, T. T., E. W. Pearl and W. E. Shenk, 1975: Satellite-tracked cumulus velocities. *J. Appl. Meteor.,* **14,** 407–413.

Gierasch, P. J., 1975: Meridional circulation and the maintenance of the Venus atmospheric rotation. *J. Atmos. Sci.,* **32,** 1038–1044.

——, 1987: Waves in the atmosphere of Venus. *Nature,* **328,** 510–512.

Guinot, B., and M. Feissel, 1968: Mesure spectrographique de

[6] *Galileo* will conduct a fly-by of Venus on its way to Jupiter and will provide some measurements in new parts of the electromagnetic spectrum.

mouvements dans l'atmosphere de Venus. *Publ. Observ. Haut-Provence,* **9,** 13–20.

Hansen, J. E., and J. W. Hovenier, 1974: Interpretation of the polarization of Venus. *J. Atmos. Sci.,* **31,** 1137–1160.

Hartley, K. H., A. R. Wolff and L. D. Travis, 1989: Croconic acid: An absorber in the Venus clouds? *Icarus,* **77,** 382–390.

Hasler, A. F., W. E. Shenk and W. C. Skillman, 1977: Wind estimates from cloud motions: Results from phases I, II, and III of an in situ aircraft verification experiment. *J. Appl. Meteor.,* **16,** 812–815.

Hendon, H. H., and D. L. Hartmann, 1985: Variability in a nonlinear model of the atmosphere with zonally symmetric forcing. *J. Atmos. Sci.,* **42,** 2783–2797.

Hou, A. Y., and R. M. Goody, 1985: Diagnostic requirements for the superrotation on Venus. *J. Atmos. Sci.,* **42,** 413–432.

——, and B. F. Farrell, 1987: Superrotation induced by critical-level absorption of gravity waves on Venus: An assessment. *J. Atmos. Sci.,* **44,** 1049–1061.

Hubert, L. F., and L. F. Whitney, 1971: Wind estimation from geostationary satellite pictures. *Mon. Wea. Rev.,* **99,** 665–672.

Ingersoll, A. P., R. F. Beebe, J. L. Mitchell, G. W. Garneau, G. M. Yagi and J.-P. Muller, 1981: Interaction of eddies and mean zonal flow on Jupiter as inferred from *Voyager 1* and *2* images. *J. Geophys. Res.,* **86,** 8733–8743.

——, ——, S. A. Collins, G. E. Hunt, J. L. Mitchell, J.-P. Muller, B. A. Smith and R. J. Terrile, 1979: Zonal velocity and texture in the Jovian atmosphere inferred from *Voyager* images. *Nature,* **280,** 773–775.

JMA, 1984: *The GMS User's Guide.* Meteorological Satellite Center, Japan Meteorological Agency, 130 pp.

Kawabata, K., D. L. Coffeen, J. E. Hansen, W. A. Lane, M. Sato and L. D. Travis, 1980: Cloud and haze properties from *Pioneer Venus* polarimetry. *J. Geophys. Res.,* **85,** 8129–8140.

Kerzhanovich, V. V., and M. Ya. Marov, 1983: The atmosphere dynamics of Venus according to Doppler measurements by the *Venera* entry probes. *Venus,* D. M. Hunten, L. Colin, T. M. Donahue and V. I. Moroz, Eds., University of Arizona, 766–778.

——, Yu. F. Makarov, M. Ya. Marov, E. P. Molotov, M. K. Rozhdestvensky, V. P. Sorokin, N. M. Antsibor, V. D. Kustodiev and V. I. Puchkov, 1979: An estimate of the wind velocity and turbulence in the atmosphere of Venus on the basis of reciprocal Doppler measurements by the *Venera 11* and *Venera 12* spacecraft. *Kosmich. Issled.,* **17,** 569–575.

Kliore, A. J., and I. R. Patel, 1980: Vertical structure of the atmosphere of Venus from *Pioneer Venus* orbiter radio occultations. *J. Geophys. Res.,* **85,** 7957–7962.

——, and ——, 1982: Thermal structure of the atmosphere of Venus from *Pioneer Venus* orbiter radio occultations. *Icarus,* **52,** 320–334.

Knollenberg, R. G., L. Travis, M. Tomasko, P. Smith, B. Ragent, L. Esposito, D. McCleese, J. Martonchik and R. Beer, 1980: The clouds of Venus: A synthesis report. *J. Geophys. Res.,* **85,** 8059–8081.

Krishnamurti, T. N., and R. J. Pasch, 1982: Large-scale mean state. *The GARP Atlantic Tropical Experiment (GATE),* Monogr., GARP Publ. Ser. No. 25, World Meteorological Organization, 27–60.

Lane, W. A., and R. Opstbaum, 1983: High altitude Venus haze from *Pioneer Venus* limb scans. *Icarus,* **54,** 48–58.

Leese, J. A., C. S. Novak and B. B. Clark, 1971: An automated technique for obtaining cloud motion from geosynchronous satellite data using cross correlation. *J. Appl. Meteor.,* **10,** 118–132.

Leovy, C. B., 1973: Rotation of the upper atmosphere of Venus. *J. Atmos. Sci.,* **30,** 1218–1220.

Limaye, S. S., 1985: Venus atmospheric circulation: Observations and implications of the thermal structure. *Adv. Space Res.,* **5,** 51–62.

——, 1988: Venus: Cloud level circulation during 1982 as determined from *Pioneer* cloud photopolarimeter images. II. Solar longitude dependent circulation. *Icarus,* **73,** 212–226.

——, and V. E. Suomi, 1981: Cloud motions on Venus: Global structure and organization. *J. Atmos. Sci.,* **38,** 1220–1235.

——, C. J. Grund and S. P. Burre, 1982a: Zonal mean circulation at the cloud level on Venus: Spring and fall 1979 OCPP observations. *Icarus,* **51,** 416–439.

——, C. Grassotti and M. J. Kuetemeyer, 1988: Venus: Cloud level circulation during 1982 as determined from *Pioneer* cloud photopolarimeter images. I. Time and zonally averaged circulation. *Icarus,* **73,** 193–211.

——, H. E. Revercomb, L. A. Sromovsky, R. J. Krauss, D. A. Santek, V. E. Suomi, S. A. Collins and C. C. Avis, 1982b: Jovian winds from *Voyager 2.* I. Zonal mean circulation. *J. Atmos. Sci.,* **39,** 1413–1432.

Linkin, V. M., V. V. Kerzhanovich, A. N. Lipatov, K. M. Pichkadze, A. A. Shurupov, A. V. Terterashvili, A. P. Ingersoll, D. Crisp, A. W. Grossman, R. E. Young, A. Seiff, B. Ragent, J. E. Blamont, L. S. Elson and R. A. Preston, 1986: VEGA balloon dynamics and vertical winds in the Venus middle cloud region. *Science,* **231,** 1417–1419.

Longuet-Higgins, M. S., 1968: The eigenfunctions of Laplace's tidal equations over a sphere. *Phil. Trans. Roy. Soc. London,* **262A,** 511–607.

Marov, M. Ya., and V. I. Moroz, 1976: Preliminary results of studies performed with space probes *Venera 9* and *Venera 10. Kosmich. Issled.,* **14,** 651–654.

Menzel, W. P., W. L. Smith and T. R. Stewart, 1983: Improved cloud motion wind vector and altitude assignment using VAS. *J. Climate Appl. Meteor.,* **22,** 377–384.

Newman, M., G. Schubert, A. J. Kliore and I. R. Patel, 1984: Zonal winds in the middle atmosphere of Venus from *Pioneer Venus* radio occultation data. *J. Atmos. Sci.,* **41,** 1901–1913.

Oort, A. H., and J. P. Peixoto, 1983: Global angular momentum and energy balance requirements from observations. *Adv. Geophys.,* **25,** 355–490.

Pechmann, J. B., and A. P. Ingersoll, 1984: Thermal tides in the atmosphere of Venus: Comparison of model results with observations. *J. Atmos. Sci.,* **41,** 3290–3313.

Preston, R. A., C. E. Hildebrand, G. H. Purcell, J. Ellis, C. T. Stelzried, S. G. Finley, R. Z. Sagdeev, V. M. Linkin, V. V. Kerzhanovich, V. I. Altunin, L. R. Kogan, V. I. Kostenko, L. I. Matveenko, S. V. Pogrebenko, I. A. Strukov, E. L. Akim, Yu. N. Alexandrov, N. A. Armand, R. N. Bakitko, A. S. Vyshlov, A. F. Bogomolov, Yu. N. Gorchankov, A. S. Selivanov, N. M. Ivanov, V. F. Tichonov, J. E. Blamont, L. Boloh, G. Laurans, A. Boischot, F. Biraud, A. Ortega-Molina, C. Rosolev and G. Petit, 1986: Determination of Venus winds by ground-based radio tracking of the VEGA balloons. *Science,* **231,** 1414–1416.

Richardson, R. S., 1958: Spectroscopic observations of Venus for rotation made at Mount Wilson in 1956. *Publ. Astron. Soc. Pac.,* **70,** 251–260.

Rind, D., and W. B. Rossow, 1984: The effects of physical processes on the Hadley circulation. *J. Atmos. Sci.,* **41,** 479–507.

Rossow, W. B., 1978: Cloud microphysics: Analysis of the clouds of Earth, Venus, Mars, and Jupiter. *Icarus,* **36,** 1–50.

——, 1983: A general circulation model of a Venus-like atmosphere. *J. Atmos. Sci.,* **40,** 273–302.

——, 1985: Atmospheric circulation of Venus. *Adv. Geophys.,* **28A,** 347–379.

——, and G. P. Williams, 1979: Large scale motion in the Venus stratosphere. *J. Atmos. Sci.,* **36,** 377–389.

——, A. D. Del Genio, S. S. Limaye, L. D. Travis and P. H. Stone, 1980: Cloud morphology and motions from *Pioneer Venus* images. *J. Geophys. Res.,* **85,** 8107–8128.

Russell, E. E., L. A. Watts, S. F. Pellicori and D. L. Coffeen, 1977: Orbiter Cloud Photopolarimeter for the *Pioneer Venus* mission. *Proc. Soc. Photo-Opt. Instrum. Eng.,* **112,** 28–44.

Sagdeev, R. Z., V. M. Linkin, J. E. Blamont and R. A. Preston, 1986a: The VEGA Venus balloon experiment. *Science,* **231,** 1407–1408.

——, ——, V. V. Kerzhanovich, A. N. Lipatov, A. A. Shurupov, J. E. Blamont, D. Crisp, A. P. Ingersoll, L. S. Elson, R. A. Preston,

C. E. Hildebrand, B. Ragent, A. Seiff, R. E. Young, G. Petit, L. Boloh, Yu. N. Alexandrov, N. A. Armand, R. V. Bakitko and A. S. Selivanov, 1986b: Overview of VEGA Venus balloon in situ meteorological measurements. *Science,* **231,** 1411–1414.

Schofield, J. T., and F. W. Taylor, 1983: Measurements of the mean solar-fixed temperature and cloud structure in the middle atmosphere of Venus. *Quart. J. Roy. Meteor. Soc.,* **109,** 57–80.

Schubert, G., 1983: General circulation and the dynamical state of the Venus atmosphere. *Venus,* D. M. Hunten, L. Colin, T. M. Donahue and V. I. Moroz, Eds., University of Arizona, 681–765.

——, C. Covey, A. Del Genio, L. S. Elson, G. Keating, A. Seiff, R. E. Young, J. Apt, C. C. Counselman, A. J. Kliore, S. S. Limaye, H. E. Revercomb, L. A. Sromovsky, V. E. Suomi, F. Taylor, R. Woo and U. van Zahn, 1980: Structure and circulation of the Venus atmosphere. *J. Geophys. Res.,* **85,** 8007–8025.

Scott, A. H., and E. J. Reese, 1972: Venus: Atmospheric rotation. *Icarus,* **17,** 589–601.

Seiff, A., D. B. Kirk, R. E. Young, R. C. Blanchard, J. T. Findlay, G. M. Kelly and S. C. Sommer, 1980: Measurements of thermal structure and thermal contrasts in the atmosphere of Venus and related dynamical observations: Results from the four *Pioneer Venus* probes. *J. Geophys. Res.,* **85,** 7903–7933.

Sill, G. T., 1983: The clouds of Venus: Sulfuric acid by the lead chamber process. *Icarus,* **53,** 10–17.

Simmons, A. J., J. M. Wallace and G. W. Branstator, 1983: Barotropic wave propagation and instability, and atmospheric teleconnection patterns. *J. Atmos. Sci.,* **40,** 1363–1392.

Smith, B. A., 1967: Rotation of Venus: Continuing contradictions. *Science,* **158,** 114–116.

Smith, E. A., and D. R. Phillips, 1972: Automated cloud tracking using precisely aligned digital ATS pictures. *IEEE Trans. Comput.,* **21,** 715–729.

Sromovsky, L. A., H. E. Revercomb and V. E. Suomi, 1985: Temperature structure in the lower atmosphere of Venus: New results derived from *Pioneer Venus* entry probe measurements. *Icarus,* **62,** 458–493.

——, ——, R. J. Krauss and V. E. Suomi, 1983: *Voyager 2* observations of Saturn's northern mid-latitude cloud features: Morphology, motions, and evolution. *J. Geophys. Res.,* **88,** 8650–8666.

Suchman, D. R., and D. W. Martin, 1976: Wind sets from SMS images: An assessment of quality for GATE. *J. Appl. Meteor.,* **15,** 1266–1278.

Suomi, V. E., 1975: *Mariner 10* observations of cloud motions. *The Atmosphere of Venus,* J. E. Hansen, Ed., NASA SP-382, 42–58.

Taylor, F. W., R. Beer, M. J. Chahine, D. J. Diner, L. S. Elson, R. D. Haskins, D. J. McCleese, J. V. Martonchik, P. E. Reichley, S. P. Bradley, J. Delderfield, J. J. Schofield, C. B. Farmer, L. Froideveaux, J. Leung, M. T. Coffey and J. C. Gille, 1980: Structure and meteorology of the middle atmosphere of Venus: Infrared remote sensing from the *Pioneer Venus* orbiter. *J. Geophys. Res.,* **85,** 7963–8006.

Tomasko, M. G., L. R. Doose, P. H. Smith and A. P. Odell, 1980: Measurements of the flux of sunlight in the atmosphere of Venus. *J. Geophys. Res.,* **85,** 8167–8186.

Toon, O. B., R. P. Turco and J. B. Pollack, 1982: The ultraviolet absorber on Venus: Amorphous sulfur. *Icarus,* **51,** 358–373.

Traub, W. A., and N. P. Carleton, 1975: Spectroscopic observations of winds on Venus. *J. Atmos. Sci.,* **32,** 1045–1059.

Travis, L. D., 1978: Nature of the atmospheric dynamics on Venus from power spectrum analysis of *Mariner 10* images. *J. Atmos. Sci.,* **35,** 1584–1595.

——, 1979: Imaging and polarimetry with the *Pioneer Venus* Orbiter Cloud Photopolarimeter. *Proc. Soc. Photo-Opt. Instrum. Eng.,* **183,** 299–304.

——, D. L. Coffeen, J. E. Hansen, K. Kawabata, A. A. Lacis, W. A. Lane, S. S. Limaye and P. H. Stone, 1979a: Orbiter cloud photopolarimeter investigation. *Science,* **203,** 781–785.

——, ——, A. D. Del Genio, J. E. Hansen, K. Kawabata, A. A. Lacis, W. A. Lane, S. S. Limaye, W. B. Rossow and P. H. Stone, 1979b: Cloud images from the *Pioneer Venus* orbiter. *Science,* **205,** 74–76.

Walterschied, R. L., G. Schubert, M. Newman and A. J. Kliore, 1985: Zonal winds and the angular momentum balance of Venus' atmosphere within and above the clouds. *J. Atmos. Sci.,* **42,** 1982–1990.

Williams, G. P., 1988: The dynamical range of global circulations—I. *Climate Dyn.,* **2,** 205–260.

——, and J. L. Holloway, 1982: The range and unity of planetary circulations. *Nature,* **297,** 295–299.

Wylie, D., and B. Hinton, 1981: The feasibility of estimating large-scale surface wind fields for the summer MONEX using cloud motion and ship data. *Bound.-Layer Meteor.,* **21,** 357–367.

Young, A. T., 1974: Is the four-day "rotation" of Venus illusory? *Icarus,* **24,** 1–10.

Young, R. E., H. Houben and L. Pfister, 1984: Baroclinic instability in the Venus atmosphere. *J. Atmos. Sci.,* **41,** 2310–2333.

——, R. L. Walterscheid, G. Schubert, A. Seiff, V. M. Linkin and A. N. Lipatov, 1987: Characteristics of gravity waves generated by surface topography on Venus: Comparison with the VEGA balloon results. *J. Atmos. Sci.,* **44,** 2628–2639.